CHEMISTRY OF MATERIALS

Article

pubs.acs.org/cm



# Transparent Conductive Two-Dimensional Titanium Carbide Epitaxial Thin Films

Joseph Halim,[†,‡,§] Maria R. Lukatskaya,[†,‡] Kevin M. Cook,[†,‡] Jun Lu,[§] Cole R. Smith,[†] Lars-Åke Näslund,[§] Steven J. May,[†] Lars Hultman,[§] Yury Gogotsi,*[,†,‡] Per Eklund,*[,§] and Michel W. Barsoum*[,†,§]

[†]Department of Materials Science & Engineering, Drexel University, Philadelphia, Pennsylvania 19104, United States

[‡]A.J. Drexel Nanomaterials Institute, Drexel University, Philadelphia, Pennsylvania 19104, United States

[§]Thin Film Physics Division, Department of Physics, Chemistry and Biology (IFM), Linköping University, SE-581 83, Linköping, Sweden

Supporting Information

**ABSTRACT:** Since the discovery of graphene, the quest for two-dimensional (2D) materials has intensified greatly. Recently, a new family of 2D transition metal carbides and carbonitrides (MXenes) was discovered that is both conducting and hydrophilic, an uncommon combination. To date MXenes have been produced as powders, flakes, and colloidal solutions. Herein, we report on the fabrication of ~1 × 1 $cm^2$ $Ti_3C_2$ films by selective etching of Al, from sputter-deposited epitaxial $Ti_3AlC_2$ films, in aqueous HF or $NH_4HF_2$. Films that were about 19 nm thick, etched with $NH_4HF_2$, transmit ~90% of the light in the visible-to-infrared range and exhibit metallic conductivity down to ~100 K. Below 100 K, the films' resistivity increases with decreasing temperature and they exhibit negative magnetoresistance—both observations consistent with a weak localization phenomenon characteristic of many 2D defective solids. This advance opens the door for the use of MXenes in electronic, photonic, and sensing applications.

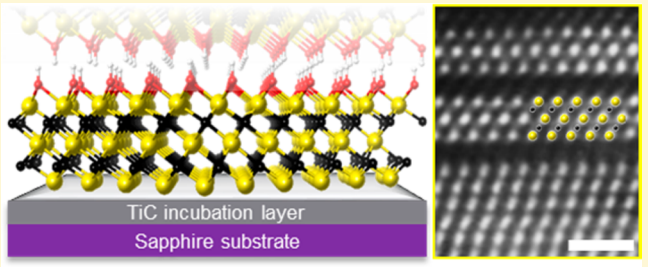


## INTRODUCTION

Since the discovery of graphene,[1−3] two-dimensional (2D) solids have attracted considerable attention due to the unique properties bestowed upon them by their reduced dimensionality. These are currently being considered for a multitude of applications, including electronic, photonic, and energy storage devices.[4−6] For instance, graphene has an electron mobility of 2 × $10^5$ $cm^2$ $V^{-1}$ $s^{-1}$ at room temperature, which shows a weak dependence on temperature.[3,7] Furthermore, a single layer of graphene transmits 97.7% of light in the near-infrared to ultraviolet range.[8] This combination of unique electronic and optical properties has positioned graphene as a promising material for transparent conductive electrodes.

The immense interest generated by graphene has renewed efforts to identify and characterize other 2D solids such as BN,[9] $MoS_2$[10,11] that may possess equally attractive properties. Recently, we discovered a new family of 2D materials that is both metallically conducting and hydrophilic, an uncommon combination indeed. This new family of materials was labeled MXenes[6,12] to emphasize that they are produced by selective etching of the A layers from the MAX phases and their similarity to graphene.[13] The latter are a large family of more than 60 phases, with the general formula of $M_{n+1}AX_n$, where $n$ = 1, 2, 3, where M is an early transition metals, A is an A-group (12−16) element, and X is carbon and/or nitrogen.[14] The MAX phases are nanolaminated, wherein every $n$-layers of M atoms are interleaved with layers of pure A; the X atoms occupy the octahedral sites between the M atoms. To date the following MXenes have been synthesized: $Ti_3C_2$,[13] $Ti_2C$, $Ta_4C_3$, TiNbC, $(V_{0.5},Cr_{0.5})_3C_2$, $Ti_3CN$,[15] and most recently $Nb_2C$ and $V_2C$.[16]

By varying the M and X elements, as well as the surface chemistries and/or the number of layers, $n$, in $M_{n+1}X_n$, it is possible to tune the MXene properties. This wealth of new 2D materials has launched experimental and theoretical activities worldwide[17,18] (see ref 12 for a recent review). MXenes show promise as anodes for lithium ion batteries; a result supported by ab initio calculations.[19−21] More recently, Lukatskaya et al.,[22] have shown that a host of cations ($Na^+$, $Mg^{2+}$, $Al^{3+}$, $NH_4^+$, etc.) can be readily intercalated, from aqueous solutions, between the $Ti_3C_2$ layers. Volumetric capacitances exceeding 300 F/$cm^3$ were reported. These values are much higher than those of porous carbon currently used in electrochemical capacitors.

However, thin films are needed to explore electronic or photonic applications. Herein, we report on the synthesis of ~1 × 1 $cm^2$ epitaxial $Ti_3C_2$ thin films. The materials described here represent a substantial advance in several ways: (1) they are produced as continuous epitaxial thin films; (2) in all previous studies, the etchant was hydrofluoric acid (HF). Here, it is

Received: February 22, 2014
Published: February 28, 2014

   dx.doi.org/10.1021/cm500641a | Chem. Mater. 2014, 26, 2374−2381

Table 1. Thickness, Etching Duration, Resistivity, and Light Transmittance (at a Wavelength of 700 nm) of the As-Deposited and Etched $Ti_3AlC_2$ Thin Films

| | | deposition time [min] | thickness [nm] | etching duration [minutes] | resistivity [$\mu\Omega$m] | transmittance [%] |
|---|---|---|---|---|---|---|
| set 1 | $Ti_3AlC_2$ | | 15.2 ± 0.5[a] | | 0.45 ± 0.01 | 31 |
| | $Ti_3C_2T_x$ | 5 | 17.2 ± 0.8[a] | 9.5 | 39.23 ± 1.21 | 68 |
| | $Ti_3C_2T_x$-IC | | 18.7 ± 0.6[a] | 150 | 4472 ± 323 | 85 |
| set 2 | $Ti_3AlC_2$ | | 27.7 ± 0.8[a] | | 0.34 ± 0.01 | 14 |
| | $Ti_3C_2T_x$ | 10 | 28.4 ± 1.8[a] | 15 | 2.28 ± 0.04 | 49 |
| | $Ti_3C_2T_x$-IC | | 31.3 ± 1.2[a] | 160 | 5.01 ± 0.03 | 37 |
| set 3 | $Ti_3AlC_2$ | | 43.4 ± 3.6[b] | | 0.31 ± 0.01 | 5.2 |
| | $Ti_3C_2T_x$ | 20 | 47.1 ± 3.5[b] | 60 | 22.27 ± 0.43 | 30 |
| | $Ti_3C_2T_x$-IC | | 52.8 ± 2.5[b] | 420 | 31 ± 2.8 | 28 |
| set 4 | $Ti_3AlC_2$ | | 60.0 ± 5.4[c] | | 0.35 ± 0.01 | 3.4 |
| | $Ti_3C_2T_x$ | 30 | 67.4 ± 5.3[c] | 160 | 1.76 ± 0.02 | 15 |
| | $Ti_3C_2T_x$-IC | | 74.7 ± 3.7[d] | 660 | 54 ± 4.51 | 14 |

[a]Determined by XRR (Supporting Information Figure S1a,b). [b]Interpolated (Supporting Information Figure S1c). [c]Obtained from direct measurement in TEM (Supporting Information Figure S9a for $Ti_3C_2T_x$). [d]Obtained from direct measurement in TEM after accounting for the decrease in thickness due to partial deintercalation.

shown that ammonium bifluoride, $NH_4HF_2$, can be used instead; (3) the one-step synthesis of a MXene, intercalated with ammonia, is demonstrated; (4) the availability of epitaxial films on transparent and insulating sapphire substrates enabled the measurement of some of the fundamental physical properties, such as optical absorption, in a broad wavelength range, and the temperature dependence of conductivity and magnetoresistance down to 2 K. These films show high transparency for wavelengths in the visible to infrared range.

## METHODS

**Deposition of $Ti_3AlC_2$.** The $Ti_3AlC_2$ thin films were deposited from three elemental targets (Ti, Al, and C with diameters of 75, 50, and 75 mm, respectively) using DC magnetron sputtering in an ultrahigh vacuum system described elsewhere.[38,39] The sputtering process gas was Ar (99.9999% purity) at a constant pressure of 4.8 mbar. The substrates were *c*-axis-oriented sapphire, $Al_2O_3$ (0001), with surface areas of 10 × 10 $mm^2$ and thicknesses of 0.5 cm (MTI Corp. CA). Prior to deposition, the substrates were cleaned using acetone, rinsed with isopropanol, dried by nitrogen gas, and finally preheated inside the deposition chamber at 780 °C for 60 min. Deposition was performed at 780 °C. Titanium and carbon targets were ignited for 5 s followed by the ignition of the aluminum target. This procedure resulted in the formation of a TiC (111) incubation layer 5−10 nm thick followed by the growth of $Ti_3AlC_2$. Previous work have shown that a TiC incubation layer facilitates the growth of epitaxial $Ti_3AlC_2$.[29,38,40]

**Synthesis of $Ti_3C_2$.** Two chemicals were used to etch, at room temperature, the $Ti_3AlC_2$ films. The first was 50% concentrated HF (Sigma Aldrich, Stockholm, Sweden). Samples of nominal thickness of 15, 28, 43, and 60 nm were etched for 10, 15, 60, and 160 min, respectively. The second was 1 M $NH_4HF_2$ (Sigma Aldrich, Stockholm, Sweden). Samples of the same thickness as those mentioned above were etched for 150, 160, 420, and 660 min, respectively. After etching, the samples were rinsed in deionized water, then in ethanol.

**Chemical and Morphological Characterization.** X-ray diffraction (XRD) of the films was performed using an X'Pert Powder diffractometer (PANalytical, Almelo, The Netherlands), with a $\theta-2\theta$ continuous scan of a step size with 0.017° and 40 s dwell time. XRD of the $Ti_3C_2T_x$-IC powders and deintercalated $Ti_3C_2T_x$ thin films were carried out using a diffractometer (SmartLab, Rigaku, Tokyo, Japan) with a $\theta$-$2\theta$ continuous scan of a step size of 0.02° and 1 s dwell time.

X-ray reflectometry (XRR) continuous scans were performed using an X'Pert Powder diffractometer (PANalytical, Almelo, The Netherlands), with a step size of 0.01° and 1.76 s dwell time. Simulation for the XRR results was carried out using the X'Pert Reflectivity software produced by PANalytical B.V.

To characterize the chemical states of elements in the thin films before and after etching, X-ray photoelectron spectroscopy (XPS) was performed using a surface analysis system (Kratos AXIS Ultra DLD, Manchester, U.K.). Monochromatic Al K$\alpha$ X-rays irradiated the samples at an angle of 45°, with respect to the surface; X-ray spot size was 300 × 800 $\mu$m. The electron energy analyzer accepted the photoelectrons perpendicular to the sample surface with an acceptance angle of ±15°. The high-resolution spectra were recorded using a pass energy of 20 eV and a step size of 0.1 eV. To avoid broadening of the XPS spectra caused by sample charging, an electron flood gun was used while recording the data. The binding energy scale of all XPS spectra was therefore referenced to the Fermi level which was set to a binding energy of 0 eV. Peak assignments of the spectra were supported through an analysis of a TiC bulk sample of known stoichiometry (1:1) and a $TiO_2$ thin film of known stoichiometry (1:2). The quantification and peak fitting were carried out using CasaXPS Version 2.3.16 RP 1.6.

Transmission electron microscopy (TEM) imaging, film thickness measurement, and selected area electron diffraction (SAED) acquisition was carried out using a TEM (FEI Tecnai G2 TF20 UT) operated at 200 kV with a point resolution of 0.19 nm. High-resolution scanning TEM imaging (HR STEM), and energy-dispersive X-ray spectroscopy (EDX) were performed using a HRTEM instrument (FEI image/probe double $C_s$ corrected Titan$^3$ G2 60−300, Eindhoven, The Netherlands) operated at 300 kV with an ultrathin window silicon drift detection X-ray energy-dispersive spectrometer and a monochromator.

Cross-sectional TEM samples were prepared by sandwiching two cross-sectioned samples in a Ti grid that was in turn mechanically polished down to 70 $\mu$m, followed by ion milling to electron transparency. Scanning electron microscopy (SEM) (Zeiss Supra 50VP, Germany) was used to investigate the morphology of the $Ti_3AlC_2$ and $Ti_3C_2T_x$ films.

**Optical and Electrical Characterization.** Transmittance values of the films were obtained using a spectrophotometer (Perkin-Elmer Lambda 950 UV−vis) with a 2-nm slit width and resolution. Spectra were corrected with both 100% and 0% transmittance background spectra. A bare sapphire substrate was used as a reference. The number of MXene layers obtained for Figure 3b were calculated by dividing the total film thicknesses by $c/2$, where $c$ is the lattice parameters obtained from XRD.

Room-temperature resistivities were measured using a four-point probe method. Three sheet-resistance measurements were taken for each sample. The errors reported in Table 1 and Supporting Information Table S4 were calculated from these three measurements.


dx.doi.org/10.1021/cm500641a | Chem. Mater. 2014, 26, 2374−2381

**Scheme 1. Steps Used to Produce Epitaxial MXene Films**[a]

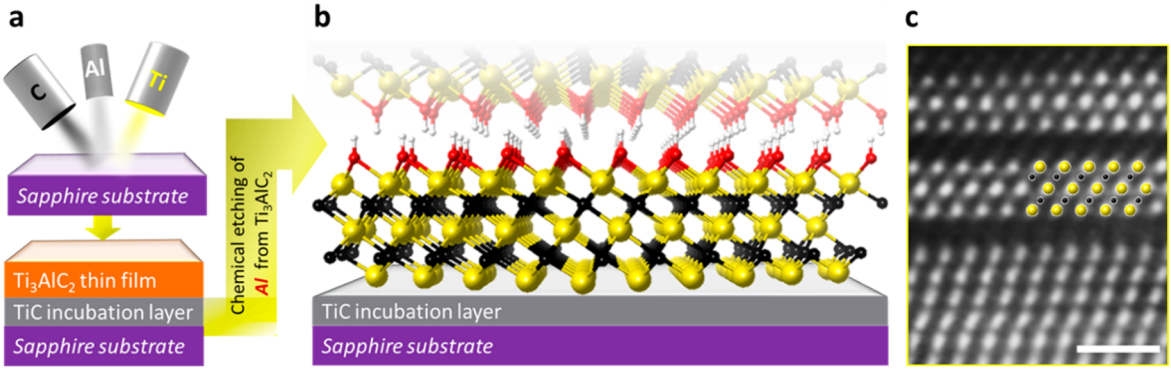


[a](a) Magnetron sputtering of Ti, Al and C forming a few-nanometer TiC incubation layer on a (0001) sapphire substrate, followed by the deposition of $Ti_3AlC_2$; (b) schematic diagram of OH-terminated $Ti_3C_2$ after selective etching of Al from $Ti_3AlC_2$ (Ti atoms are yellow, C atoms are black, O atoms are red, and H atoms are white); (c) STEM image of the first two $Ti_3C_2T_x$ layers after applying Wiener filter; scale bar is equal to 1 nm. Inset shows Ti atoms in yellow and C atoms in black.

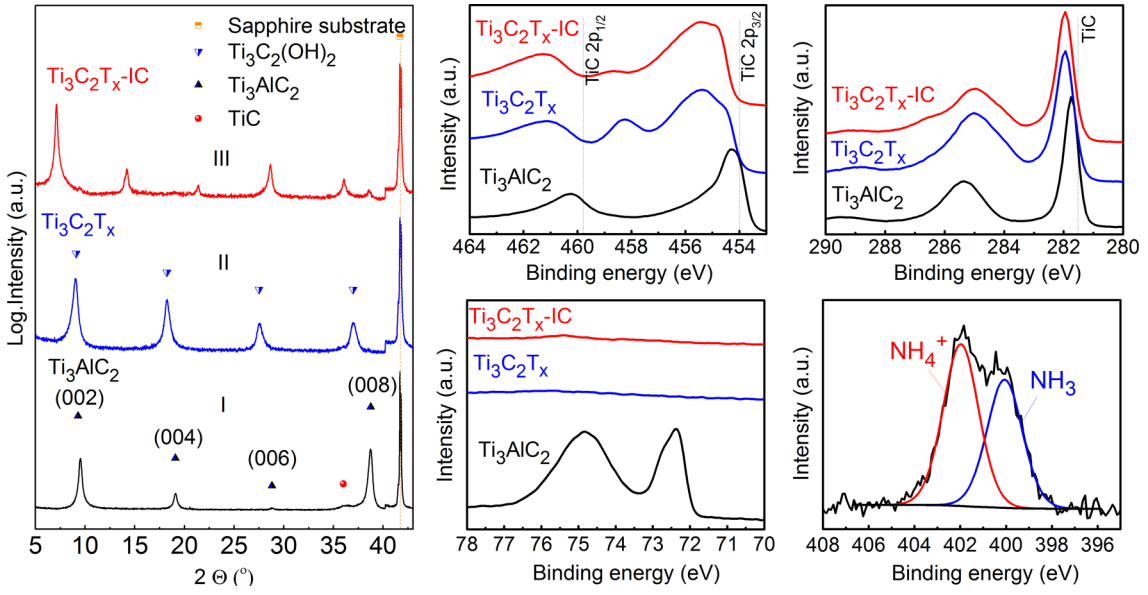


**Figure 1.** (a) XRD patterns of as-deposited −60 nm nominal thickness - $Ti_3AlC_2$ thin films (I), $Ti_3C_2T_x$ after etching in 50% HF for 2 h 40 min (II), and $Ti_3C_2T_x$-IC after etching in 1 M $NH_4HF_2$ for 11 h (III). XPS spectra of, (b) Ti 2p, (c) C 1s, and (d) Al 2p for $Ti_3AlC_2$, $Ti_3C_2T_x$, and $Ti_3C_2T_x$-IC thin films, respectively. The vertical lines in panels b and c indicate the positions of Ti (3/2p and 1/2p) and C (1s) binding energies in TiC, respectively. (e) High resolution XPS spectra for N 1s region for $Ti_3C_2T_x$-IC, best fitted by symmetric Gaussian−Lorentzian curves resting on a Shirley background. The two components correspond to $(NH_4^{+1})$[24] and $(NH_3)$.[25]

The resistivity was obtained by multiplying the sheet resistance with the corresponding average film thickness.

The temperature-dependent in-plane resistivity measurements were performed in a Physical Property Measurement System (Quantum Design, San Diego) using an external current source (Keithley 6220, Ohio) and a nanovoltmeter (Keithley 2182A). A linear four-point probe geometry was used. Gold wires were attached to the films using silver paint. Positive and negative currents were applied at each temperature to eliminate any thermal offsets. The magnetoresistance, MR, measurements were performed with the magnetic field—up to 10 T—applied out of the plane of the film.

## ■ RESULTS AND DISCUSSION

The films used were 15 to 60 nm thick $Ti_3AlC_2$ films deposited onto sapphire (000*l*) substrates by magnetron sputtering. More details can be found in Supporting Information Section I. Scheme 1a shows the process starting from the sputter-deposition of $Ti_3AlC_2$ (with initial formation of a TiC incubation layer). This is followed by etching of the Al layers resulting in 2D $Ti_3C_2T_x$ layers (Scheme. 1b), where $T_x$ stands for the surface −O, −OH, or −F terminations resulting from the aqueous HF etchant. In Scheme 1b, the $Ti_3C_2$ surfaces are presumed to be OH-terminated. STEM image of the interface between the TiC incubation layer and $Ti_3C_2T_x$ is shown in Scheme 1c. The fact that the very first MXene layer has an ordered structure bodes well for the production of single layer MXene films.

To date, the only etchant reported for producing MXenes has been HF.[13,15,16] Herein, we show that, $NH_4HF_2$ can be used for the same purpose. The main advantage of the latter is that it is less hazardous than HF[23] and is a milder etchant. Its use leads to the concomitant intercalation of cations during the etching process. For the sake of brevity, these films will be referred to as $Ti_3C_2T_x$-IC, where the IC represents the intercalated species, viz. $NH_3$ and $NH_4^+$ (see below).


dx.doi.org/10.1021/cm500641a | Chem. Mater. 2014, 26, 2374−2381

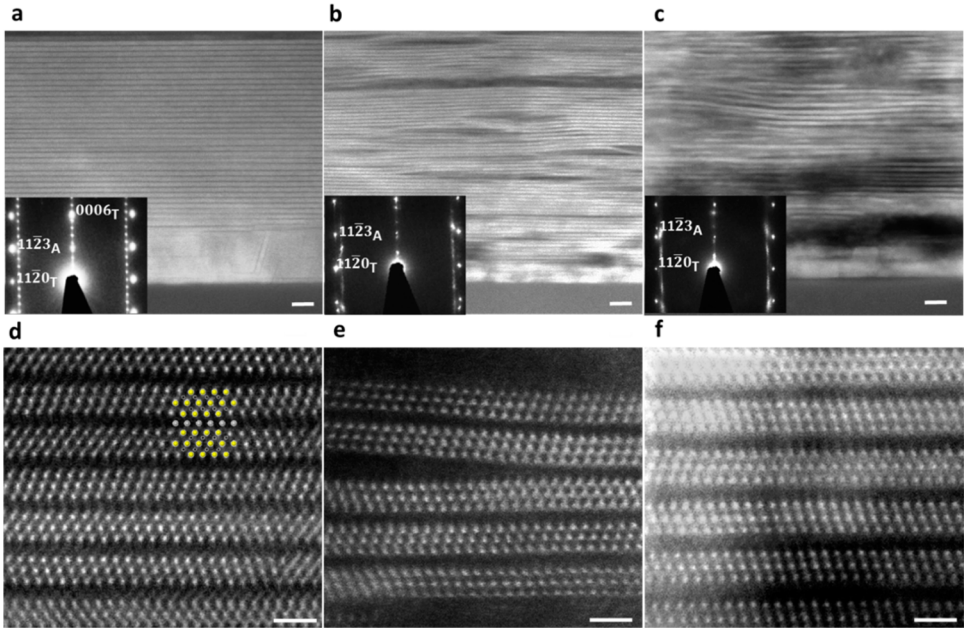


**Figure 2.** Cross-sectional STEM images of (a) $Ti_3AlC_2$, (b) $Ti_3C_2T_x$, (c) and $Ti_3C_2T_x$-IC films (60 nm nominal thickness) grown on a sapphire substrate with a TiC incubation layer. Insets show SAED of the film and the substrate. The subscripts A and T correspond to $Al_2O_3$ and $Ti_3AlC_2$, respectively. High-resolution STEM images of (d) $Ti_3AlC_2$, (e) $Ti_3C_2T_x$, and (f) $Ti_3C_2T_x$-IC films along the [11$\bar{2}$0] zone axis. The inset in panel d shows Ti, Al, and C atoms in yellow, gray, and black, respectively. Scale bars for low resolution (a, b, and c) and high-resolution (d, e, and f) images correspond to 5 and 1 nm, respectively.

A typical XRD pattern of an as-deposited $Ti_3AlC_2$ film (Figure 1a, I) shows the (000*l*) peaks from $Ti_3AlC_2$, a TiC incubation layer) and the sapphire substrate.[23] The presence of only peaks corresponding to basal-plane oriented $Ti_3AlC_2$ indicates epitaxial growth, a fact also confirmed by TEM and SAED (Figure 2a). The $Ti_3C_2T_x$ XRD pattern (Figure 1a, II) on the other hand, shows a shift to a lower angles of the 000*l* peaks corresponding to an increase in the *c* lattice parameter from 18.6 Å for $Ti_3AlC_2$ to 19.8 Å for $Ti_3C_2T_x$. The latter value agrees with previous work on $Ti_3C_2T_x$ synthesized from $Ti_3AlC_2$ powders.[13] The XRD pattern of $Ti_3C_2T_x$-IC (Figure 1a, III), is similar to the other two, except that now *c* is further increased to 24.7 Å.

Similar behavior was observed when $Ti_3AlC_2$ powders were intercalated with $NH_4OH$ or $NH_4F$ after HF etching. In both cases, the *c* lattice expansion was of the order of 25% (see Supporting Information Figure S5a). The independence of the increase in the *c* lattice parameter on the nature of the anion of the etching solution strongly suggests that the cations ($NH_4^+$) and/or ($NH_3$), and not the anions, are the intercalated species. We note in passing that the present work is in contradistinction to the recent work by Lukatskaya et al. who intercalated $NH_4OH$ into $Ti_3C_2T_x$,[22] in a two-step process. Herein, the etching and intercalation occur in a single step. This is an important result because it considerably simplifies the intercalation process.

The XPS results, shown in Figure 1b–d for films, with a nominal thickness of 60 nm, demonstrate a shift in the Ti 2p and C 1s (Figure 1b and c) toward higher binding energies for the titanium carbide species in $Ti_3AlC_2$, $Ti_3C_2T_x$, and $Ti_3C_2T_x$-IC, compared to those of binary TiC (shown in Figure 1b and c as thin vertical lines), indicating the change in the nature of bonding between the Ti and C atoms in $Ti_3AlC_2$ and the corresponding MXenes. The latter most likely occurs because valence electrons are withdrawn from the Ti atoms, and subsequently from the C atoms, in the MXene layers by the surface functional groups, as well as from the interaction of the surface with the intercalated compounds. The removal of Al is verified by the high-resolution spectra in the Al 2p region for $Ti_3C_2T_x$ and $Ti_3C_2T_x$-IC (Figure 1d), in which a very weak Al signal—most probably originating from aluminum fluoride (see Supporting Information section I)—is recorded. The $Ti_3AlC_2$, Al 2p signal corresponds to Al bonded to Ti, as well as, to surface aluminum oxide.

The reactions of HF with $Ti_3AlC_2$ have been postulated by Naguib et al.[15] to be

$$Ti_3AlC_2 + 3HF = AlF_3 + 3/2H_2 + Ti_3C_2 \quad (1)$$

$$Ti_3C_2 + 2H_2O = Ti_3C_2(OH)_2 + H_2 \quad (2)$$

$$Ti_3C_2 + 2HF = Ti_3C_2F_2 + H_2 \quad (3)$$

Reaction 1 is followed by reactions 2 and 3, which result in OH and F terminated $Ti_3C_2$ surfaces or $Ti_3C_2T_x$. The elemental ratio obtained from the analysis of high-resolution (XPS) spectra is $Ti_3C_{2.2}O_2F_{0.6}$ (see Supporting Information section II). As indicated by XPS, terminal hydroxyl and fluoride groups exist on the surface of the material, thereby indirectly confirming the aforementioned reactions. EDX mapping in the TEM (Supporting Information Figure S7) also confirms the presence of F and O atoms between the $Ti_3C_2$ layers.

As discussed above for the $NH_4HF_2$ etched $Ti_3AlC_2$, the etching of the Al and the intercalation of ammonium species occur concomitantly. It is thus reasonable to conclude that in this case the following reactions are operative:

$$Ti_3AlC_2 + 3NH_4HF_2 = (NH_4)_3AlF_6 + Ti_3C_2 + \frac{3}{2}H_2 \quad (4)$$


dx.doi.org/10.1021/cm500641a | *Chem. Mater.* 2014, 26, 2374–2381

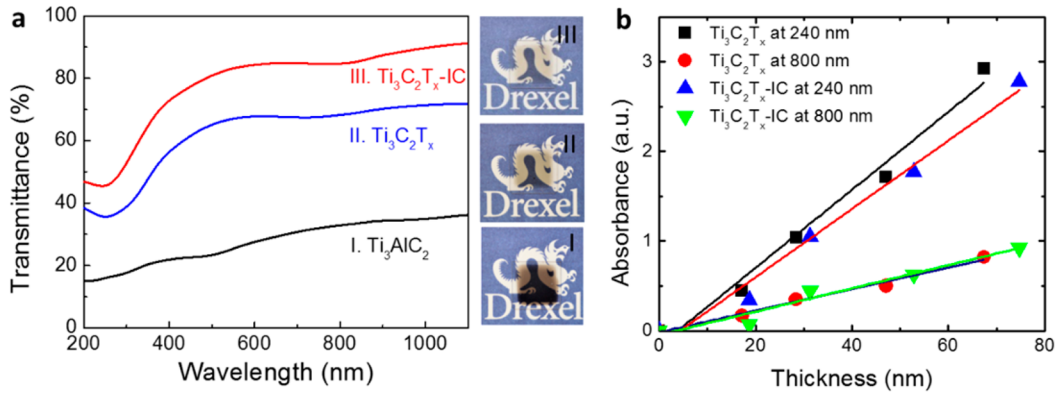


**Figure 3.** (a) Transmittance spectra and visual images (on right) for (I) $Ti_3AlC_2$, (II) $Ti_3C_2T_x$, and (III) $Ti_3C_2T_x$-IC films of 15 nm nominal thickness. The films are ≈1 × 1 $cm^2$ in area; (b) light absorbance at wavelengths of 240 and 800 nm vs thickness of $Ti_3C_2T_x$ and $Ti_3C_2T_x$-IC films.

$$Ti_3C_2 + aNH_4HF_2 + bH_2O = (NH_3)_c(NH_4)_dTi_3C_2(OH)_xF_y \quad (5)$$

Unlike HF etching, $NH_4HF_2$ etching results in formation of $(NH_4)_3AlF_6$ according to reaction 4 (see Supporting Information section III). Reaction 5 depicts the intercalation of $NH_3$ and $NH_4^{+1}$ between the $Ti_3C_2T_x$ layers.[26] In order to confirm the nature of the intercalating species in $Ti_3C_2T_x$-IC, a high-resolution XPS spectrum of the N 1s region was recorded (Figure 1e). The latter was best fitted by two components: one for $NH_4^{+1}$ (55.8% of N 1s; peak position, 402 eV; fwhm, 1.8 eV);[24] the other for $NH_3$ (44.2% of N 1s; peak position, 400.1 eV; fwhm, 1.8 eV).[25] It is thus reasonable to conclude that both species intercalate this MXene. We note in passing that both $NH_3$ and $NH_4^+$ intercalate between the 2D layers of transition metal dichalcogenides, such as $TiSe_2$ and $TiS_2$.[27,28]

The elemental ratio obtained from the analysis of high-resolution XPS spectra (see Supporting Information section II) of $Ti_3C_2$ produced by $NH_4HF_2$ etching is $Ti_3C_{2.3}O_{1.2}F_{0.7}N_{0.2}$. Here again, the XPS analysis indicates the presence of terminal hydroxyl and fluoride groups.

Cross-sectional scanning TEM micrographs of as-deposited $Ti_3AlC_2$ films, before (Figure 2a and d) and after etching with HF (Figure 2b and e) or $NH_4HF_2$ (Figure 3c and f) clearly show the presence of the TiC incubation layers and the effects of etching on the microstructures of the films. The SAED patterns confirm the out-of-plane epitaxial relationship $Ti_3AlC_2(0001)//TiC(111)//Al_2O_3(0001)$.[29] At 18.6 Å, the *c* lattice parameter for $Ti_3AlC_2$, obtained from the SAED pattern and TEM micrographs (see Supporting Information section VIII), is in excellent agreement with that calculated from XRD (18.6 Å). At 19.5−20 Å, the *c* lattice parameters of $Ti_3C_2T_x$ obtained from the SAED patterns match the ones obtained from XRD (19.8 Å). However, at 21 ± 0.5 Å, the average *c* for $Ti_3C_2T_x$-IC measured from the SAED pattern is considerably lower than that obtained from XRD (25 Å). The most probable reason for this state of affairs is the deintercalation of the ammonium species during TEM sample preparation and/or observation (see Methods and Supporting Information section IV).

The light elements of the surface termination groups (O, H, and F) cannot be seen between the layers, but the larger and nonuniform spacing seen in Figure 2b, c, e, and f indirectly confirm the weak interactions between the MXene layers after etching and the formation of a 2D structure. The nonuniform interlayer spacing observed in the STEM images of the HF-etched sample (Figure 2b) could also account for the peak broadening observed in XRD (Figure 2a).

Prior to etching, the initial thicknesses of the films examined in TEM were 60 nm (Figure 2a). However, as a result of the increase in *c* and the separation between the MXene layers, due to exfoliation, the etched films were thicker than the initial films (Table 1). Comparing the atomic layers in $Ti_3C_2T_x$-IC (Figure 2c and f) to those of the $Ti_3C_2T_x$ layers (Figures 3b, and e), it is obvious that the former are more uniformly spaced. This result most probably reflects the milder nature of $NH_4HF_2$ as compared to HF. For the latter, the reaction is faster (Table 1) and more vigorous than the former. Another possible explanation is that the intercalation of ammonia species leads to stronger interactions between MXene layers, essentially "gluing" them together as observed for other MXene intercalation compounds.[22,30]

In terms of light transmittance, both $Ti_3C_2T_x$ and $Ti_3C_2T_x$-IC films are significantly more transparent than $Ti_3AlC_2$ of the same initial thickness, 15 nm (Figure 3a, and Table 1). The increased transparency of $Ti_3C_2T_x$ and $Ti_3C_2T_x$-IC, compared to that of $Ti_3AlC_2$ is also evident visually (Figure 3, middle insets).

With 90% transmittance, the $Ti_3C_2T_x$-IC films were the most transparent, followed by the $Ti_3C_2T_x$ films at 70%. With a transmittance of 30%, the $Ti_3AlC_2$ films were the least transparent. It is worth noting here that the transmittance of all films would have been higher had the TiC incubation layer been absent.

A linear dependence of the absorbance—that is independent of the wavelength of the light—on the thickness of the $Ti_3C_2T_x$ and $Ti_3C_2T_x$-IC films was observed (Figure 3b). Given the similarities in the transmittance curves and the linear dependencies of absorbance values for both samples, it is reasonable to conclude that $Ti_3C_2T_x$ and $Ti_3C_2T_x$-IC are quite similar in structure. A crude estimation of the transmittance of a single MXene layer, *d*, (since each length *c* is comprised of two MXene layers, *d* is approximately equal to the film thickness divided by 2*c*) could be obtained from the linear fits of absorbance vs *d*. The transmittances, calculated at a wavelength of 240 nm, for single layers of $Ti_3C_2T_x$ and $Ti_3C_2T_x$-IC are about 90.5% and 91.5%, respectively; the corresponding transmittances, at a wavelength of 800 nm, are 97.3% and 97.1% respectively. The latter values are quite close to those reported for graphene single layers.[8] Note that to obtain these values, both the thickness and absorbance of the TiC incubation layer were neglected.


dx.doi.org/10.1021/cm500641a | *Chem. Mater.* 2014, 26, 2374−2381

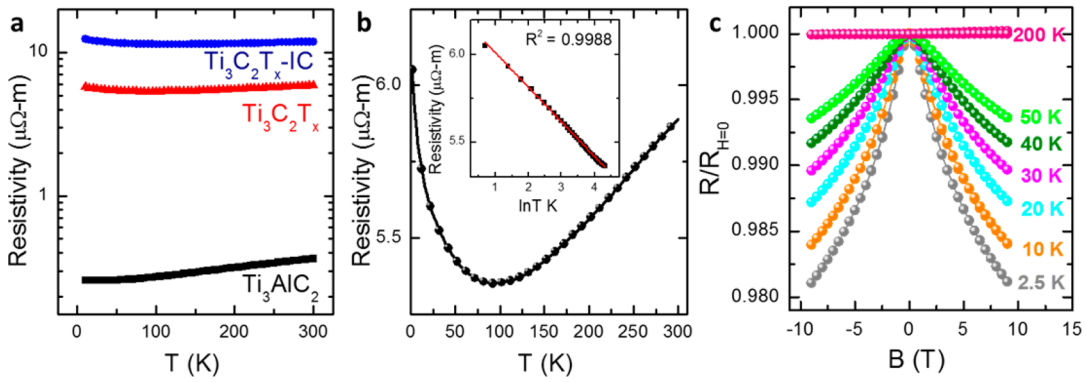


**Figure 4.** Dependence of the electrical behavior of $Ti_3AlC_2$, $Ti_3C_2T_x$, and $Ti_3C_2T_x$-IC films on temperature and magnetic field. (a) Resistivity vs temperature for $Ti_3AlC_2$, $Ti_3C_2T_x$, and $Ti_3C_2T_x$–IC films of 20 nm nominal thickness. (b) Resistivity vs temperature for $Ti_3C_2T_x$ of 28 nm nominal thickness. Inset shows fitting of resistivity, over the temperature range of 2 to 74 K, to the weak localization model ($\rho \sim \ln T$). (c) Comparison of normalized magnetoresistance curves for $Ti_3C_2T_x$ of 28 nm nominal thickness at various temperatures ranging from 2.5 to 200 K. $R_{H=0}$ refers to the film resistance in the absence of applied magnetic field.

We next turn to the electrical properties, which confirm the metallic-like nature of the conductivities of all etched films despite their optical transparency. As expected, and consistent with previous work,[31] the $Ti_3AlC_2$ films are metallic with resistivity, $\rho$, values in the range from 0.37 to 0.45 $\mu\Omega$ m. The latter increase linearly with increasing temperature (Figure 3a). Furthermore, $\rho$ increases with decreasing film thickness (Table 1 and Supporting Information Figure S10). The resistivity values of the $Ti_3C_2T_x$-IC films are systematically higher than those produced by HF etching. For instance, 28 nm nominally thick $Ti_3C_2T_x$ and $Ti_3C_2T_x$-IC films have $\rho$ values of 2.3 and 5.0 $\mu\Omega$ m, respectively. This result is also consistent with previous work that has shown that intercalation of MXenes with organic compounds increases their resistivity.[30] The resistivities of the etched films also depend significantly on etching time; longer etching times lead to higher $\rho$ values presumably due to the formation of defects (see Supporting Information Table S2), in agreement with previous work.[32] The results listed in Table 1 are those obtained upon the full MAX to MXene conversion. The latter was determined by intermittently etching each film, followed by XRD. When the $Ti_3AlC_2$ peaks disappeared, the etching process was halted (Supporting Information Figure S6). We note in passing that there were no changes in the $c$ lattice parameter with etching time. Furthermore, the fact that the conductivities are affected by the intercalants, suggests that MXenes can potentially be used as sensors.

At 1.8 $\mu\Omega$ m, a 60 nm nominally thick $Ti_3C_2T_x$ sample is the most conductive of the HF etched films $Ti_3C_2T_x$ films (Table 1). However, at 700 nm wavelength, its transmittance is only 15%. The 15 nm nominally thick $Ti_3C_2T_x$ sample exhibited the highest transmittance (68% at 700 nm wavelength) with a $\rho$ of 39.2 $\mu\Omega$ m. For the $Ti_3C_2T_x$-IC films, the lowest resistivity was 5.0 $\mu\Omega$ m, with a transmittance of about 37%; the most transparent (>85% at 700 nm wavelength) had a resistivity of ≈4.5 m$\Omega$ m.

At this juncture, it is worth comparing our results with other conductive electrodes at a wavelength of 550 nm. Referring to Supporting Information Figure S10, it is obvious that while the transmittance of our thinnest films is higher than that of indium tin oxide, ITO, their sheet resistance values are orders of magnitude higher. When compared to graphene transparent conductive electrodes, again MXene transmittance values are slightly higher, but the resistivity is about 2 orders of magnitude higher.

Why the resistivities measured herein are as high as they are, is unclear at this time. One possibility is the film morphology. As noted above, the $Ti_3AlC_2$ films are predominantly $c$-axis oriented (Figure 2a). However, a secondary grain population, whose basal planes are not parallel to the substrate, also exists (see Supporting Information Figure S9). If the reasonable assumption is made that after etching the conductivity along [0001] is significantly lower than along [100], this secondary grain population, will act as insulating islands. Reducing the fraction of such grains should result in films that are more conductive when etched. Deintercalation of films by heat treatment can alone increase the conductivity by an order of magnitude or more.[30]

Theoretical calculations predict that it is possible to alter the electronic properties of MXenes by altering their surface terminations.[21,33] For example, pure $Ti_3C_2$ is predicted to exhibit a metallic behavior, whereas $Ti_3C_2F_2$ and $Ti_3C_2(OH)_2$ are predicted to have band gaps of 0.05 and 0.1 eV, respectively.[4,13] Thus, another potential avenue for enhancing the films' conductivities is to eliminate the surface groups. We note in passing that several applications, such as touch screen, electromagnetic shielding for cathode ray tubes and electrostatic dissipation, require sheet resistance values which are comparable to what we report for MXene thin films, viz. 1000 to 1 M$\Omega$/sq.[34]

To elucidate the conduction mechanisms of the MXene layers, their resistivities, and magnetoresistances (MRs) from room temperature down to about 2.5 K were measured. Figure 4a shows the temperature dependent resistivity for $Ti_3AlC_2$, $Ti_3C_2T_x$, and $Ti_3C_2T_x$-IC films of 28 nm nominal thickness. The $Ti_3AlC_2$ films exhibit metallic behavior from 300 K down to about 10 K. For the $Ti_3C_2T_x$ and $Ti_3C_2T_x$-IC films, on the other hand, metallic behavior is observed from 300 to about 100 K; below 100 K the resistivity increases with decreasing temperature (Figure 4b). Similar low-temperature behavior was observed in other $Ti_3C_2T_x$ and $Ti_3C_2T_x$-IC films (see Supporting Information Figure S11). The low temperature transport data can best be fit assuming $\rho \sim \ln T$ (inset in Figure 4b). As shown in Supporting Information Figure S7, other mechanisms associated with insulating behavior, such as thermally activated processes, 3D variable range hopping and others, do not accurately reflect the $\rho$ (T) data (see Supporting Information Figure S12). The logarithmic dependence on temperature is consistent with weak localization, a phenomen-


dx.doi.org/10.1021/cm500641a | Chem. Mater. 2014, 26, 2374−2381

on caused by electron backscattering and often observed in 2D metals.[35] To provide further insight into the transport properties, MR measurements were performed in the low temperature ($d\rho/dT < 0$) and high temperature ($d\rho/dT > 0$) regimes. The appearance of negative MR in the low temperature regime (Figure 4c) is again consistent with weak localization, verifying that these materials are indeed 2D.[35−37]

## CONCLUSIONS

In conclusion, epitaxial $Ti_3C_2T_x$ films can be readily produced by the room temperature etching of epitaxial $Ti_3AlC_2$ thin films in HF or $NH_4HF_2$ solutions. The latter etchant yields films intercalated with $NH_3$ and $NH_4^+$ species, that have $c$ lattice parameters (∼ 25 Å) that are 25% larger than films etched with HF. The $Ti_3C_2T_x$-IC films have higher transparencies and resistivities than their $Ti_3C_2T_x$ counterparts. $Ti_3C_2T_x$ and $Ti_3C_2T_x$-IC films of ∼15-nm nominal thickness were found to be 68 and 85% transparent, respectively. Both films also exhibited metallic conductivity down to 100 K; below 100 K, the resistivities increase with decreasing temperatures and exhibit negative MRs at the lowest temperatures, both attributes consistent with, and evidence for, their 2D metallic nature.

The MXene films produced herein are promising materials for transparent conductive electrodes, sensors and other applications. By better control of the deposition process, such that nonbasal growth is eliminated or minimized, the potential exists for enhancing their conductivities. A parallel approach is to modify, or eliminate, the surface terminations such as F, O, or OH.

Synthesis of single-layer $Ti_3C_2$ films is the next frontier. Other MXenes (Ti-based and others containing other transition metals such as Nb, V, Ta, etc. or nitrogen in addition to carbon) may also show attractive optical and electrical properties and should be produced and studied in their thin-film state. It is vital to note here that the production of epitaxial uniform multilayer MXene films is a necessary and crucial first step to applying this novel and unique family of materials in the field of electronics, optoelectronics and photonics. Given the vast richness of MXene chemistries, together with the multiple different intercalants (from cations to polymers to organic molecules), it is obvious that we are standing at the edge of a truly vast *terra incognita*.

## ASSOCIATED CONTENT

### Supporting Information

XRR, thickness determination, XPS analysis of $Ti_3AlC_2$, $Ti_3C_2T_x$ and $Ti_3C_2T_x$-IC thin films, XRD analysis of byproducts from etching $Ti_3AlC_2$ with $NH_4HF_2$, intercalation and deintercalation of $Ti_3C_2T_x$ thin films, optimization of the etching process, EDX mapping of $Ti_3C_2T_x$, SEM and TEM for $Ti_3AlC_2$ and $Ti_3C_2T_x$ thin films, and electrical transport measurements and analysis. This material is available free of charge via the Internet at http://pubs.acs.org.

## AUTHOR INFORMATION


### Corresponding Authors

*E-mail: barsoumw@drexel.edu.
*E-mail: perek@ifm.liu.se.
*E-mail: gogotsi@drexel.edu.


### Author Contributions

J.H. planned and performed the thin film depositions; performed and developed the etching process; performed XRD of the films before and after etching; and measured the room temperature resistivities. M.R.L. performed the intercalation and deintercalation experiments; carried out the XRD scans and analysis of the intercalated, and deintercalated samples; performed the SEM; and made the figures for the manuscript. K.M.C. measured and analyzed the optical transmittance properties. C.R.S. and S.J.M. performed and analyzed the temperature dependent resistivity and MR measurements. J.L. performed and analyzed the TEM micrographs with contributions from J.H., L.H., and P.E. XPS experiments were performed by L.-Å.N. Additionally, J. H. analyzed the results with contributions from K.M.C. and L.-Å.N. The manuscript draft was written by J.H. and P.E. All authors were involved in the discussions and commented on and revised successive drafts of the manuscript. M.W.B., L.H., and Y.G. conceived and initiated the research. M.W.B, L.H., Y.G., and P.E. supervised the work.

### Notes

The authors declare no competing financial interest.

## ACKNOWLEDGMENTS


Hossein Fashandi is acknowledged for his help and useful discussions about growth of $Ti_3AlC_2$ thin films. The authors acknowledge funding from the Swedish Research Council (VR) Grant Nos. 621-2012-4430 and 621-2011-4420, the VR Linnaeus Strong Research Environment LiLi-NFM. M.W.B., J.H., and P.E. also acknowledge the Swedish Foundation for Strategic Research (SSF) through the Synergy Grant FUNCASE (M.W.B., J.H., and P.E.) and the Ingvar Carlsson Award 3 (P.E.). The Knut and Alice Wallenberg Foundation supported the Ultra-Electron Microscopy Laboratory at Linköping University operated by the Thin Film Physics Division. S.J.M. and C.R.S. were supported by the U.S. Office of Naval Research (ONR N00014-11-1-0109); the acquisition of the Physical Properties Measurement System was supported by the U.S. Army Research Office under grant number W911NF-11-1-0283. M.L. and Y.G. were supported by the US Department of Energy, Energy Storage Systems Research Program through Sandia National Laboratory.


## REFERENCES


(1) Novoselov, K. S.; Geim, A. K.; Morozov, S. V.; Jiang, D.; Zhang, Y.; Dubonos, S. V.; Grigorieva, I. V.; Firsov, A. A. *Science* **2004**, *306*, 666−669.

(2) Novoselov, K.; Jiang, D.; Schedin, F.; Booth, T.; Khotkevich, V.; Morozov, S.; Geim, A. *Proc. Natl. Acad. Sci. U.S.A.* **2005**, *102*, 10451−10453.

(3) Novoselov, K. S.; Fal'ko, V. I.; Colombo, L.; Gellert, P. R.; Schwab, M. G.; Kim, K. *Nature* **2012**, *490*, 192−200.

(4) Tang, Q.; Zhou, Z. *Progress in Materials Science* **2013**, *58*.

(5) Nicolosi, V.; Chhowalla, M.; Kanatzidis, M. G.; Strano, M. S.; Coleman, J. N. *Science* **2013**, *340*, 1420−1438.

(6) Zhang, X.; Xie, Y. *Chem. Soc. Rev.* **2013**, *42*, 8187−8199.

(7) Bolotin, K. I.; Sikes, K. J.; Jiang, Z.; Klima, M.; Fudenberg, G.; Hone, J.; Kim, P.; Stormer, H. L. *Solid State Commun.* **2008**, *146*, 351−355.

(8) Nair, R. R.; Blake, P.; Grigorenko, A. N.; Novoselov, K. S.; Booth, T. J.; Stauber, T.; Peres, N. M.; Geim, A. K. *Science* **2008**, *320*, 1308.

(9) Ci, L.; Song, L.; Jin, C.; Jariwala, D.; Wu, D.; Li, Y.; Srivastava, A.; Wang, Z. F.; Storr, K.; Balicas, L.; Liu, F.; Ajayan, P. M. *Nat. Mater.* **2010**, *9*, 430−435.

(10) van der Zande, A. M.; Huang, P. Y.; Chenet, D. A.; Berkelbach, T. C.; You, Y.; Lee, G. H.; Heinz, T. F.; Reichman, D. R.; Muller, D. A.; Hone, J. C. *Nat. Mater.* **2013**, *12*, 554−561.
(11) Najmaei, S.; Liu, Z.; Zhou, W.; Zou, X.; Shi, G.; Lei, S.; Yakobson, B. I.; Idrobo, J. C.; Ajayan, P. M.; Lou, J. *Nat. Mater.* **2013**, *12*, 754−759.
(12) Naguib, M.; Mochalin, V. N.; Barsoum, M. W.; Gogotsi, Y. *Adv. Mater.* **2014**, *26*, 992−1005.
(13) Naguib, M.; Kurtoglu, M.; Presser, V.; Lu, J.; Niu, J.; Heon, M.; Hultman, L.; Gogotsi, Y.; Barsoum, M. W. *Adv. Mater.* **2011**, *23*, 4248−4253.
(14) Barsoum, M. W. *MAX Phases: Properties of Machinable Ternary Carbides and Nitrides*; John Wiley & Sons: New York, 2013.
(15) Naguib, M.; Mashtalir, O.; Carle, J.; Presser, V.; Lu, J.; Hultman, L.; Gogotsi, Y.; Barsoum, M. W. *ACS Nano* **2012**, *6*, 1322−1331.
(16) Naguib, M.; Halim, J.; Lu, J.; Cook, K. M.; Hultman, L.; Gogotsi, Y.; Barsoum, M. W. *J. Am. Chem. Soc.* **2013**, *135*, 15966−15969.
(17) Enyashin, A.; Ivanovskii, A. *J. Solid State Chem.* **2013**, *207*, 42−48.
(18) Enyashin, A. N.; Ivanovskii, A. L. *J. Phys. Chem. C* **2013**, *117*, 13637−13643.
(19) Naguib, M.; Come, J.; Dyatkin, B.; Presser, V.; Taberna, P. L.; Simon, P.; Barsoum, M. W.; Gogotsi, Y. *Electrochem. Commun.* **2012**, *16*, 61−64.
(20) Tang, Q.; Zhou, Z.; Shen, P. *J. Am. Chem. Soc.* **2012**, *134*, 16909−16916.
(21) Shein, I. R.; Ivanovskii, A. L. *Micro Nano Lett.* **2013**, *8*, 59−62.
(22) Lukatskaya, M. R.; Mashtalir, O.; Ren, C. E.; Dall'Agnese, Y.; Rozier, P.; Taberna, P. L.; Naguib, M.; Simon, P.; Barsoum, M. W.; Gogotsi, Y. *Science* **2013**, *341*, 1502−1505.
(23) Misra, A.; Prasad, J.; Sees, J. A.; Hall, L. H. Benign Method for Etching Silicon Dioxide. U.S. Patent No. 6048406, 2000.
(24) Bourbigot, S.; Le Bras, M.; Gengembre, L.; Delobel, R. *Appl. Surf. Sci.* **1994**, *81*, 299−307.
(25) Egawa, C.; Naito, S.; Tamaru, K. *Surf. Sci.* **1983**, *131*, 49−60.
(26) Rakov, E. G. e.; Mel'nichenko, E. *Russ. Chem. Rev.* **1984**, *53*, 851−869.
(27) Friend, R. H.; Yoffe, A. D. *Adv. Phys.* **1987**, *36*, 1−94.
(28) Bernard, L.; Mckelvy, M.; Glaunsinger, W.; Colombet, P. *Solid State Ionics* **1985**, *15*, 301−310.
(29) Wilhelmsson, O.; Palmquist, J.-P.; Lewin, E.; Emmerlich, J.; Eklund, P.; Persson, P.; Högberg, H.; Li, S.; Ahuja, R.; Eriksson, O. *J. Cryst. Growth* **2006**, *291*, 290−300.
(30) Mashtalir, O.; Naguib, M.; Mochalin, V. N.; Dall'Agnese, Y.; Heon, M.; Barsoum, M. W.; Gogotsi, Y. *Nat. Commun.* **2013**, *4*, 1716.
(31) Wilhelmsson, O.; Palmquist, J.-P.; Nyberg, T.; Jansson, U. *Appl. Phys. Lett.* **2004**, *85*, 1066−1068.
(32) Mashtalir, O.; Naguib, M.; Dyatkin, B.; Gogotsi, Y.; Barsoum, M. W. *Mater. Chem. Phys.* **2013**, *139*, 147−152.
(33) Khazaei, M.; Arai, M.; Sasaki, T.; Chung, C. Y.; Venkataramanan, N. S.; Estili, M.; Sakka, Y.; Kawazoe, Y. *Adv. Funct. Mater.* **2013**, *23*, 2185−2192.
(34) Geng, H.-Z.; Kim, K. K.; So, K. P.; Lee, Y. S.; Chang, Y.; Lee, Y. H. *J. Am. Chem. Soc.* **2007**, *129*, 7758−7759.
(35) Bergmann, G. *Phys Rev B* **1982**, *25*, 2937−2939.
(36) Bergmann, G. *Phys. Rep.* **1984**, *107*, 1−58.
(37) Henzler, M.; Lüer, T.; Heitmann, J. *Phys Rev B* **1999**, *59*, 2383−2387.
(38) Emmerlich, J.; Högberg, H.; Sasvári, S.; Persson, P. O. Å.; Hultman, L.; Palmquist, J.-P.; Jansson, U.; Molina-Aldareguia, J. M.; Czigány, Z. *J. Appl. Phys.* **2004**, *96*, 4817−4826.
(39) Frodelius, J.; Eklund, P.; Beckers, M.; Persson, P.; Högberg, H.; Hultman, L. *Thin Solid Films* **2010**, *518*, 1621−1626.
(40) Eklund, P.; Beckers, M.; Frodelius, J.; Högberg, H.; Hultman, L. *J. Vac. Sci. Technol., A* **2007**, *25*, 1381−1388.

# Supporting Information

# Transparent Conductive Two-Dimensional Titanium Carbide Epitaxial Thin Films

*Joseph Halim,[†,‡,§] Maria R. Lukatskaya,[†,‡] Kevin M. Cook,[†,‡] Jun Lu,[§] Cole R. Smith,[†] Lars-Åke Näslund,[§] Steven J. May,[†] Lars Hultman,[§] Yury Gogotsi,[†,‡,*] Per Eklund,[§,*] and Michel W. Barsoum[†,§,*]*

[†]Department of Materials Science & Engineering, Drexel University, Philadelphia, PA 19104, USA.

[‡]A.J. Drexel Nanomaterials Institute, Drexel University, Philadelphia, PA 19104, USA. Department of Materials Science & Engineering, Drexel University, Philadelphia, PA 19104, USA.

[§]Thin Film Physics Division, Department of Physics, Chemistry and Biology (IFM), Linköping University, SE-581 83, Linköping, Sweden.

barsoumw@drexel.edu; perek@ifm.liu.se; gogotsi@drexel.edu

## I. X-ray reflectometry and thickness determination

Films' thickness has been determined from XRR for $Ti_3AlC_2$ films, before and after etching, deposited for 5 and 10 min, examples of the XRR data and their fittings shown in Figures S1, and S2. For $Ti_3AlC_2$ film deposited for 30 mins, thicknesses before and after etching were obtained by direct measurement in TEM (Figures 2a-c, and Figure S9c). Figure S1 shows the measured X-Ray reflectometry for $Ti_3AlC_2$ (black curve), and best-fitted simulation from TiC incubation layer/$Ti_3AlC_2$ (red curve): for a film deposited for 5 min (Figure S1a) giving a thickness of 15.2 ± 0.5 nm and a film deposited for 10 min (Figure S1b) giving a thickness of 27.7 ± 0.8 nm. Figure S1c shows the relationship between the thickness of $Ti_3AlC_2$, $Ti_3C_2T_x$ and $Ti_3C_2T_x$-IC and deposition time of $Ti_3AlC_2$. Films deposited for 20 min: their thickness before and after etching was obtained from interpolation (Figure S3c).

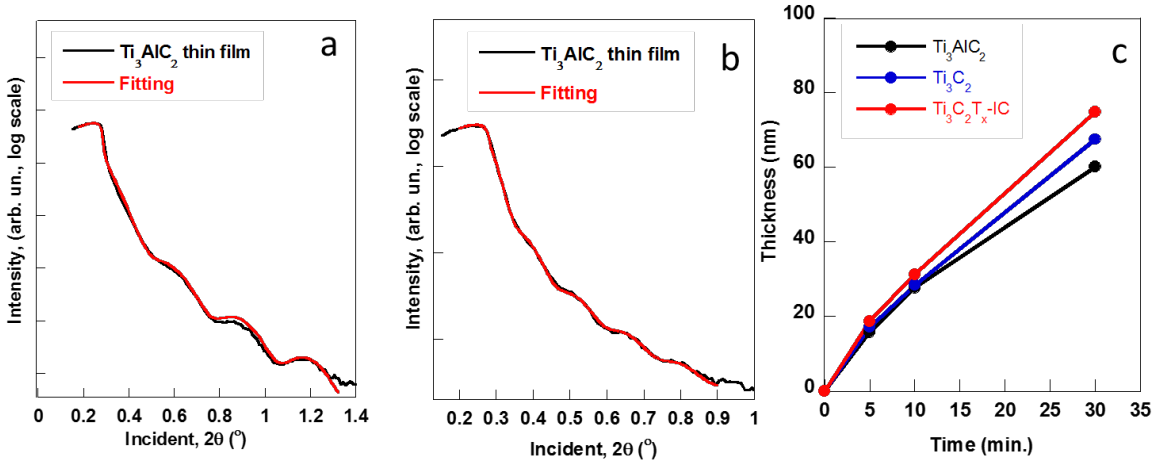


**Figure S1.** Measured X-Ray reflectometry for (a) $Ti_3AlC_2$ sputtered for 5 min and, (b) $Ti_3AlC_2$ sputtered for 10 min, $Ti_3AlC_2$ (black curve), and best fit simulation for TiC incubation layer/ $Ti_3AlC_2$ (red curve) and (c) Thickness *vs.* deposition time of $Ti_3AlC_2$ for $Ti_3AlC_2$, $Ti_3C_2T_x$ and $Ti_3C_2T_x$-IC.

## II. XPS analysis of $Ti_3AlC_2$, $Ti_3C_2T_x$, and $Ti_3C_2T_x$-IC

Analysis of the high-resolution XPS spectra was performed through peak fitting using symmetric Gaussian-Lorentzian curves resting on a Shirley background.

Fig. S2 presents the Ti 2p, C 1s, and Al 2p regions for the $Ti_3AlC_2$ thin film together with the obtained Shirley background and Gaussian-Lorentzian curves for each region. In the Ti 2p region (Figure S2a), which contains both the $2p_{1/2}$ and the $2p_{3/2}$ spin-orbit split components, the XPS spectrum could be best fit with four pairs of Gaussian-Lorentzian curves, where each pair is the $2p_{1/2}$ and the $2p_{3/2}$ component that we assign to Ti-Al, Ti-C, Ti(II) oxide, and Ti(III) oxide, respectively.[1-4]

The C 1s region (Figure S2b) could be fit with four Gaussian-Lorentzian curves. The low binding energy feature is a sharp asymmetric peak that is assigned to the Ti-C bond.[1,2] The asymmetry is due to extrinsic energy losses caused by delocalized states. This asymmetry, in turn, required the Ti-C XPS peak to be fit with two symmetric Gaussian-Lorentzian curves. In addition to the Ti-C peak there are two peaks assigned to surface hydrocarbon (-$CH_2$- & -$CH_3$) and carboxylate (-COO)[5] contamination common for samples exposed to laboratory air.[6]

In the Al 2p region (Figure S2c) the low binding energy feature contains the $2p_{1/2}$ and the $2p_{3/2}$ spin-orbit split components assigned to Ti-Al.[3] The high binding energy feature is assigned to an aluminum oxide components,[2] fitted with a symmetric Gaussian-Lorentzian curve, due to surface oxidation which is common for MAX phase materials.[2] The results obtained from the peak fitting of the $Ti_3AlC_2$ thin film are summarized in Table S1.

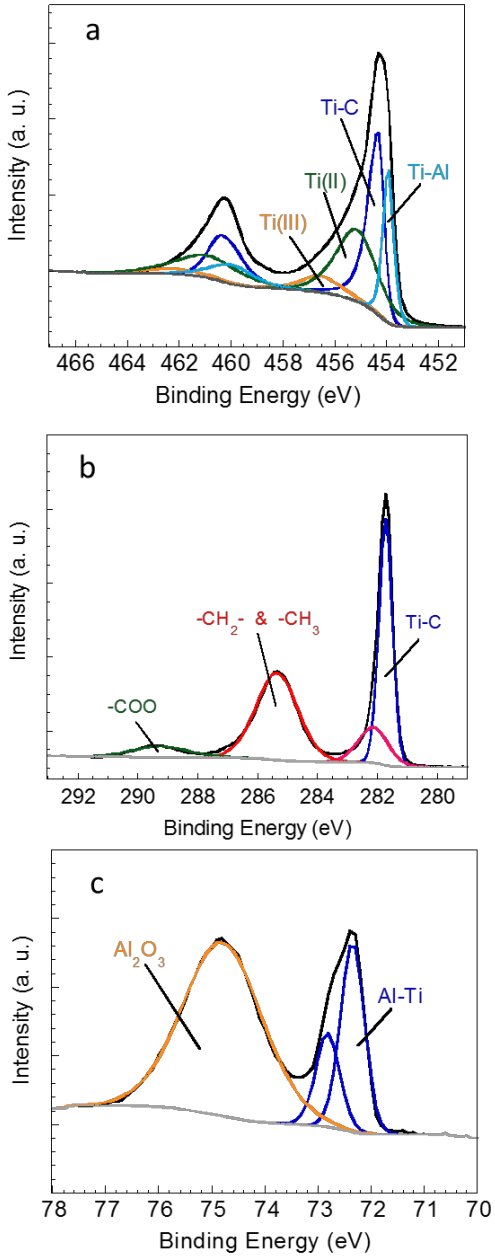


**Figure S2.** Deconvolution of high resolution XPS spectra for elements in $Ti_3AlC_2$ films. (a) Ti 2p, (b) C 1s and (c) Al 2p XPS high resolution spectra for $Ti_3AlC_2$ thin films.

**Table S1**. $Ti_3AlC_2$ XPS peak fitting results. Parameters obtained from the peak fitting of the $Ti_3AlC_2$ thin film XPS spectra using symmetric Gaussian-Lorentzian curves.

| | BE [eV][a] | fwhm [eV][a] | Fraction | Assigned to | Reference |
|---|---|---|---|---|---|
| Ti $2p_{3/2}$ ($2p_{1/2}$) | 453.9 (459.9) | 0.5 (2.0) | 0.20 | Ti-Al | [3] |
| | 454.3 (460.3) | 0.5 (1.3) | 0.37 | Ti-C | [1, 2] |
| | 455.2 (460.9) | 1.9 (3.0) | 0.35 | Ti(II) oxide | [4] |
| | 456.5 (462.1) | 1.9 (3.0) | 0.08 | Ti(III) oxide | [4] |
| C 1s | 281.7 | 0.5 | 0.38 | Ti-C | [1, 2] |
| | 282.1 | 1.2 | 0.13 | Ti-C | |
| | 285.3 | 1.7 | 0.43 | $-CH_2-$ & $-CH_3$ | [5] |
| | 289.3 | 1.7 | 0.06 | -COO | [5] |
| Al $2p_{3/2}$ ($2p_{1/2}$) | 72.4 (72.8) | 0.5 (0.5) | 0.33 | Ti-Al | [3] |
| | 74.8 (74.8) | 1.7 | 0.66 | $Al_2O_3$ | [5] |

[a]Values in parenthesis corresponds to the $2p_{1/2}$ component.

Figures S3a-d and Figures S3e-h represent the Ti 2p, C 1s, O 1s, and F 1s regions for the $Ti_3C_2T_x$ thin film and the $Ti_3C_2T_x$-IC thin film, respectively. For both MXene thin films, the XPS spectrum of the Ti 2p region (Figures S3a, and S3e) could be best fitted with five pairs of Gaussian-Lorentzian curves, where each pair is the $2p_{1/2}$ and the $2p_{3/2}$ component that we assign to Ti-C, Ti(II) oxide, Ti(III) oxide, Ti(IV) oxide, and Ti-F, respectively.[3-5,7-9] The C 1s region for both MXene thin films (Figures S3b, and S3f) shows features assigned to Ti-C,[1, 2] hydrocarbons ($-CH_2-$ & $CH_3-$), and carboxylates (-COO). In this case intense contributions from graphite (C-C) and alcohol (C-O) formation are also present.[5]

The O 1s region for both MXene thin films (Figures S3c, and S3g) could be fit by two components assigned to titanium oxide: one component for stoichiometric $TiO_2$ and one component for sub-stoichiometric $TiO_x$.[9] The O 1s region also suggests Ti-OH formation and $H_2O$ uptake.[9]

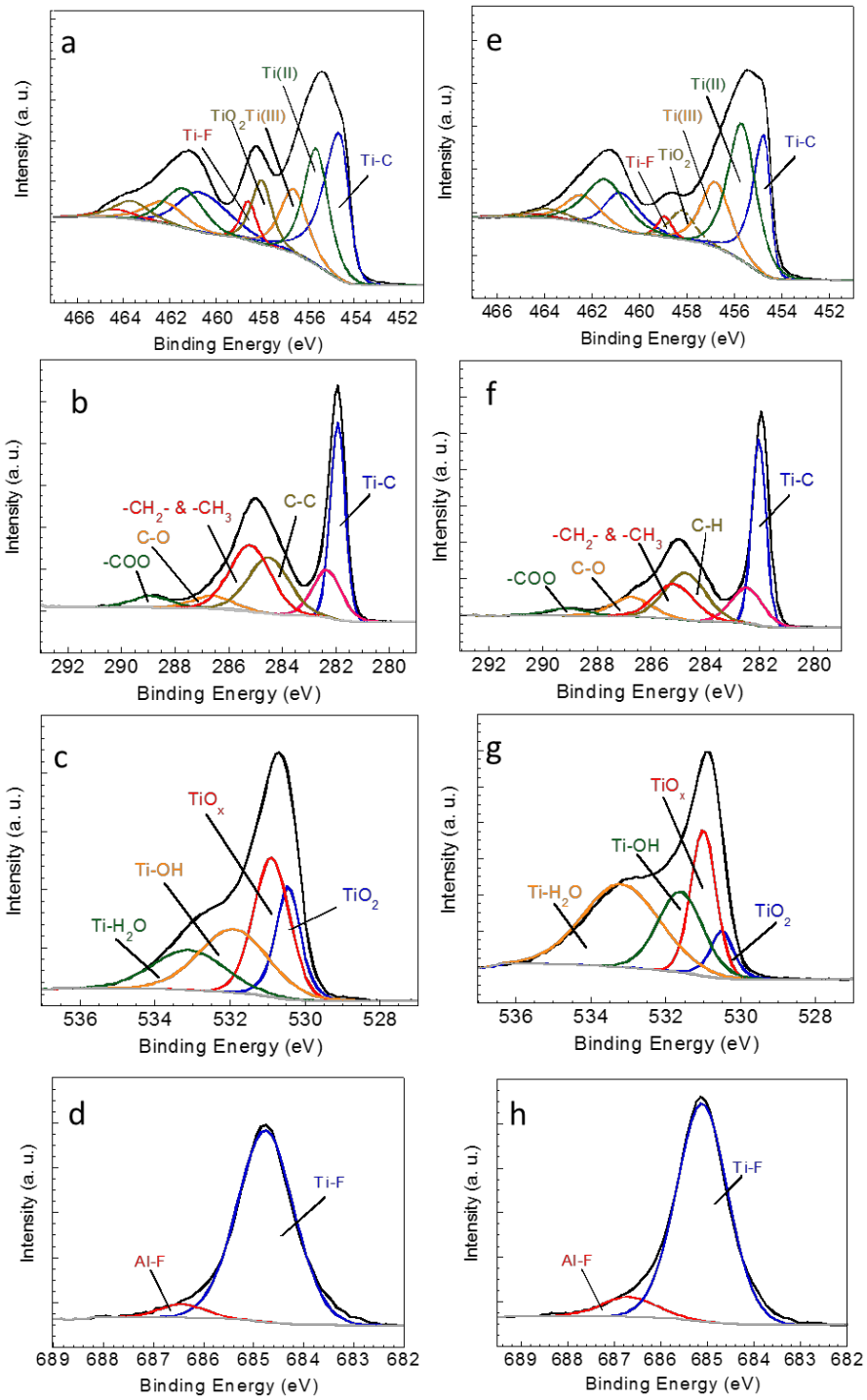


**Figure S3.** Deconvolution of high resolution XPS spectra for elements in $Ti_3C_2T_x$, and $Ti_3C_2T_x$-IC. (a) Ti 2p, (b) C 1s, (c) O 1s and, (d) F 1s regions for $Ti_3C_2T_x$ C; and, (e) Ti 2p; f, (f) 1s, (g) O 1s and, (h) F1s regions for $Ti_3C_2T_x$-IC thin films.

The F 1s region for both MXene thin films (Figs. S3d and S3h) shows a dominating contribution from fluorinated titanium,[8] Ti-F, but also a small component assigned to aluminum fluoride,[10] Al-F, which is corroborated by the appearance of a weak feature at

73.6 eV in the Al 2p spectra shown in Figure 2b. The results obtained from the peak fitting of the $Ti_3C_2T_x$ thin film and the $Ti_3C_2T_x$-IC thin film are summarized in Tables S2 and S3.

**Table S2.** $Ti_3C_2T_x$ XPS peak fitting result. Parameters obtained from the peak fitting of the $Ti_3C_2T_x$ thin film XPS spectra using symmetric Gaussian-Lorentzian curves.

| | BE [eV][a] | fwhm [eV][a] | Fraction | Assigned to | Reference |
|---|---|---|---|---|---|
| Ti $2p_{3/2}$ ($2p_{1/2}$) | 454.6 (460.7) | 0.9 (2.2) | 0.37 | Ti-C | [1, 2,7] |
| | 455.6 (460.9) | 1.3 (2.0) | 0.28 | Ti(II) oxide | [4, 7] |
| | 456.6 (462.2) | 1.4 (2.0) | 0.17 | Ti(III) oxide | [7] |
| | 458.0 (463.7) | 1.0 (1.8) | 0.12 | Ti(IV) oxide | [10,9] |
| | 458.6 (464.3) | 0.8 (1.8) | 0.06 | Ti-F | [8] |
| C 1s | 281.9 | 0.6 | 0.25 | Ti-C | [1, 2] |
| | 282.3 | 1.3 | 0.15 | Ti-C | |
| | 284.5 | 1.6 | 0.15 | C-C | [5] |
| | 285.2 | 1.6 | 0.34 | $-CH_2-$ & $-CH_3$ | [5] |
| | 286 .6 | 1.6 | 0.07 | C-O | [5] |
| | 288.9 | 1.6 | 0.04 | -COO | [5] |
| O 1s | 530.5 | 0.8 | 0.21 | $TiO_2$ | [9] |
| | 531.0 | 1.1 | 0.33 | $TiO_x$ | [9] |
| | 531.8 | 2.0 | 0.25 | Ti-OH | [9] |
| | 533 | 2.2 | 0.21 | Ti-$H_2O$ | [9] |
| F 1s | 684.7 | 1.3 | 0.95 | Ti-F | [8] |
| | 686.4 | 1.1 | 0.05 | Al-F | [10] |

[a]Values in parenthesis corresponds to the $2p_{1/2}$ component.

**Table S3.** $Ti_3C_2T_x$-IC XPS peak fitting result. Parameters obtained from the peak fitting of the $Ti_3C_2T_x$-IC thin film XPS spectra using symmetric Gaussian-Lorentzian curves.

| | BE [eV][a] | fwhm [eV][a] | Fraction | Assigned to | Reference |
|---|---|---|---|---|---|
| Ti $2p_{3/2}$ | 454.7 (460.8) | 0.7 (1.5) | 0.29 | Ti-C | [1, 2, 7] |
| ($2p_{1/2}$) | 455.7 (461.4) | 1.4 (2.0) | 0.41 | Ti(II) oxide | [4, 7] |
| | 456.8 (462.4) | 1.4 (1.8) | 0.20 | Ti(III) oxide | [7] |
| | 458.2 (463.9) | 1.2 (1.9) | 0.07 | Ti(IV) oxide | [10,9] |
| | 458.9 (464.6) | 0.7 (1.9) | 0.03 | Ti-F | [8] |
| C 1s | 281.9 | 0.6 | 0.29 | Ti-C | [1, 2] |
| | 282.3 | 1.4 | 0.14 | Ti-C | |
| | 284.6 | 1.8 | 0.21 | C-C | [5] |
| | 285.2 | 1.8 | 0.21 | C-H | [5] |
| | 286.6 | 1.8 | 0.11 | C-O | [5] |
| | 289.0 | 1.8 | 0.04 | -COO | [5] |
| O 1s | 530.5 | 0.7 | 0.08 | $TiO_2$ | [9] |
| | 530.9 | 0.8 | 0.25 | $TiO_x$ | [9] |
| | 532.5 | 1.4 | 0.25 | Ti-OH | [9] |
| | 533.1 | 2.4 | 0.42 | Ti-$H_2O$ | [9] |
| F 1s | 685.3 | 1.3 | 0.91 | Ti-F | [8] |
| | 686.7[b] | 1.4 | 0.09 | Al-F | [10] |

[a]Values in parenthesis corresponds to the $2p_{1/2}$ component.
[b]The peak for the aluminum fluoride component shifts to a higher binding energy compared to that for $Ti_3C_2T_x$, while its FWHM maximum increases, which may be due to the formation of $(NH_4)_3AlF_6$ rather than $AlF_3$ as indicted by XRD in Figure S6.

The high-resolution XPS spectra of the Ti 2p and C 1s regions for the $Ti_3AlC_2$, $Ti_3C_2T_x$, and $Ti_3C_2T_x$-IC thin films show that the removal of Al causes a shift of the Ti-C contribution in the Ti 2p and C 1s XPS spectra toward higher binding energies, indicative of a loss of charge, and a concomitant charge redistribution within the material. Note that this decrease of charge is not due to the removal of Al atoms, because the latter needs to leave behind the charge they gained when forming $Ti_3AlC_2$. The charge redistribution is instead a consequence of the higher electronegativities of the OH, O and F surface functional groups, as mentioned in the main text.

In addition there is a slight shift to higher binding energies for the Ti 2p spectrum of the $Ti_3C_2T_x$-IC thin film compared to the corresponding spectrum of $Ti_3C_2T_x$. Since the matching C 1s spectra do not show any changes in the binding energies, the observed binding energy shift could be due to the intercalated nitrogen species (Figure 2e) interacting with the surface of the $Ti_3C_2T_x$-IC thin film.

The peak fitting of the XPS high-resolution spectra suggests the chemical compositions to be $Ti_3C_{2.2}O_2F_{0.6}$ and $Ti_3C_{2.3}O_{1.2}F_{0.7}N_{0.2}$ for $Ti_3C_2T_x$ and $Ti_3C_2$-IC, respectively. Fitted peaks that correspond to surface oxidation and contamination, i.e. $TiO_2$, $H_2O$, hydrocarbons, alcohols, carboxylates, and aluminum fluoride, are not included in these elemental quantifications. The obtained quantification data indicates that the etching of $Ti_3AlC_2$, using HF or $NH_4HF_2$, provides near-stoichiometric $Ti_3C_2$ 2D-stuctures, surface terminated with a mixture of fluoride- and hydroxyl groups. Additionally, etching in $NH_4HF_2$ results in the intercalation of the nitrogen species, $NH_4^+$ and $NH_3$.[11,12]

## III. XRD analysis of the byproducts from etching $Ti_3AlC_2$ with $NH_4HF_2$

One half of a gram of $Ti_3AlC_2$ powder (the method of preparation is described elsewhere[13]) were soaked in 5ml of 1M $NH_4HF_2$ solution at room temperature. The mixture was left untouched until the solvent evaporated. XRD diffraction of the dry powders (Figure S4) indicates the existence of two byproduct compounds $(NH_4)_3AlF_6$ (PDF# 22-1036) and $AlF_3.3H_2O$ (PDF# 46-1459) comparing the intensity of the maximum peaks for both gives a ratio of about 7:1 respectively. It follows that the major byproduct from etching $Ti_3AlC_2$ with $NH_4HF_2$ is $(NH_4)_3AlF_6$.

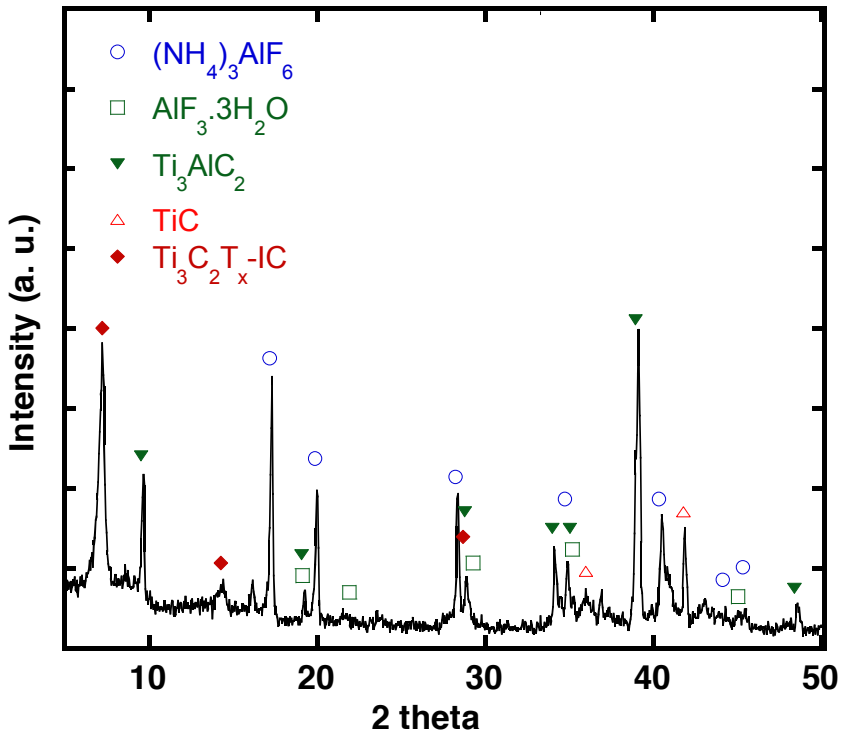


**Figure S4:** X-Ray diffraction pattern of $Ti_3C_2T_x$ intercalated MXene ($Ti_3C_2T_x$-IC) after etching $Ti_3AlC_2$ powder with 1M $NH_4HF_2$, and allowing the mixture to sit until the solvent dried. In contrast to our previous work, here the resulting salt was not washed away with water. The XRD pattern also includes peaks associated with un-reacted $Ti_3AlC_2$ and TiC present as an impurity in the as-received powders.

## IV. Intercalation and de-intercalation of $Ti_3C_2T_x$

In order to verify the assumption that intercalation is the pertinent mechanism, $Ti_3C_2$ powder (the method of preparation is described elsewhere[13]) were immersed in 1 M of $NH_4F$ or in 5 M $NH_4OH$ for 24 h at room temperature while stirring. XRD patterns before and after treatment, shown in Fig. S5a, confirm that the increase in *c*, from 19.8 Å to 25 Å, in both solutions is similar to that observed when $NH_4HF_2$ was used as etchant. It is thus reasonable to assume that, intercalant compound should be the common species between $NH_4HF_2$, $NH_4F$ and $NH_4OH$, viz. $NH_4^+$.

To investigate the reversibility of the intercalation process, a 43 nm nominal thickness $Ti_3C_2T_x$-IC film was heated in a vacuum at 250 °C for 90 min. The XRD patterns for the film before and after de-intercalation are compared in Figure S5b. After the vacuum treatment, the (0002) peak shifts to an angle that corresponds to a *c* lattice parameter of 21 Å. It is thus possible to de-intercalate ammonia from $Ti_3C_2T_x$-IC. This value is also quite similar to, the lattice parameter obtained from SAED pattern shown in Figure 3e, suggesting that the TEM sample was partially de-intercalated during the sample preparation.

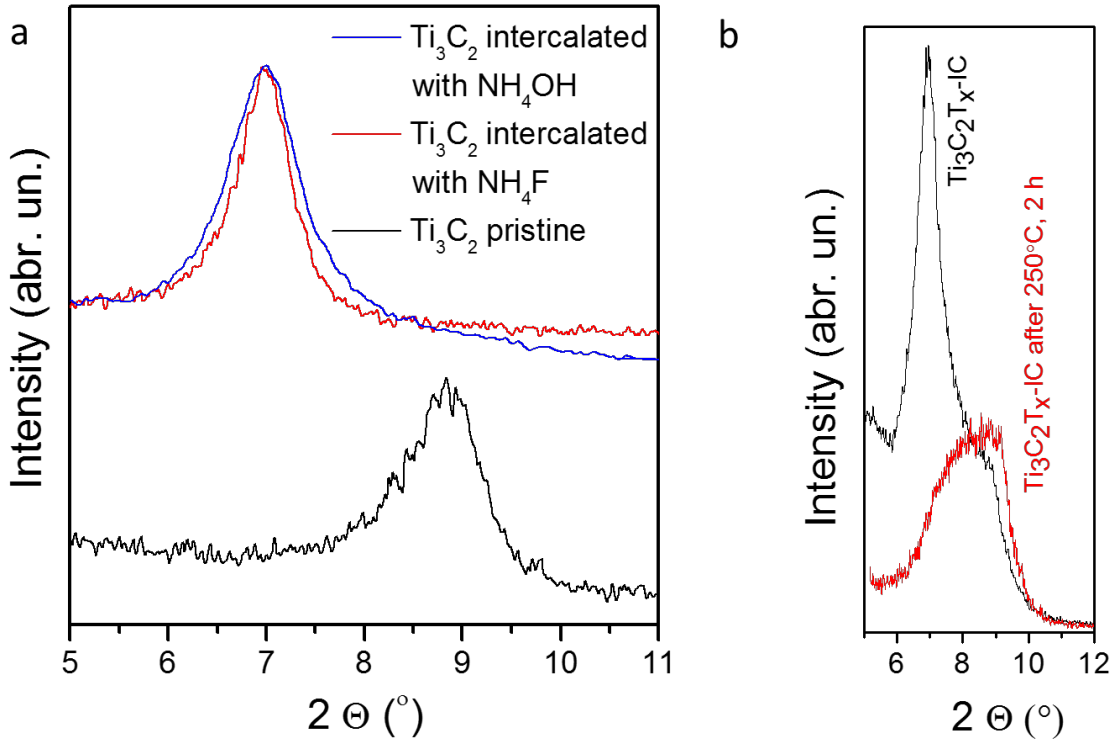


**Figure S5.** (a) X-Ray diffraction pattern of initial MXene ($Ti_3C_2T_x$) powder (black curve), and after 24 h treatment at room temperature with 1 M $NH_4F$ (red curve) and 5 M $NH_4OH$ (blue curve). (b) $Ti_3C_2T_x$-IC film of 43 nm nominal thickness before and after heating in vacuum at 250 °C for 2 h.

## V. Optimization of the etching process

The resistivities of all films increased with increase in etching times. Table S4 lists the resistivities of $Ti_3C_2T_x$ films produced by HF etching for samples, of the same nominal thicknesses, etched for different times. For example, the resistivities of $Ti_3AlC_2$ films, 60 nm nominal thick, etched for 160 mins and 360 mins were 1.8 μΩm and 3.4 μΩm, respectively.

The etching time required to fully transform the $Ti_3AlC_2$ films to MXenes was determined by repeatedly measuring the XRD diffraction patterns, of a given film, after successive etching steps until the XRD peaks belonging to $Ti_3AlC_2$ disappeared (Figure S6). This procedure was adopted in order to compare the properties of all etched films at the point all the Al layers were etched out. Said otherwise, the etching times varied from film to film. The dependence is not linear, however. For example, the etching times for $Ti_3AlC_2$ films of nominal thicknesses 15 and 28 nm were 10 and 15 mins, respectively. Similarly, at 150 min and 160 min, the time needed to fully etch 15 nm and 28 nm thick $Ti_3AlC_2$ films in $NH_4HF_2$, were quite comparable (See Table 1).

A perusal of the results shown in Tables 1 and S4 suggest that the final resistivities one obtains is a complicated function of film thickness, etching times and the nature of the etchant. On the one hand, thin films are more resistive than their thicker counterparts. It is this variability - reflected in Table 1 - that is most probably responsible for some of the

anomalies observed. For example, the etching times for $Ti_3C_2T_x$ films of nominal thicknesses of 15, 28 and 43 nm were 10, 15 and 60 min, respectively.

**Table S4:** Resistivity of $Ti_3AlC_2$ films after etching in 50% HF for various times. The thicknesses listed in the first column are thicknesses before etching

| Thickness [nm] | Etching time [minutes] | Resistivity [μΩm] |
|---|---|---|
| 10 | 9.5 | 39 ± 1.21 |
| | 60 | 1820 ± 150 |
| 40 | 60 | 22 ± 0.4 |
| | 360 | 42 ± 3.3 |
| 60 | 160 | 1.8 ± 0.1 |
| | 360 | 3.4 ± 0.1 |

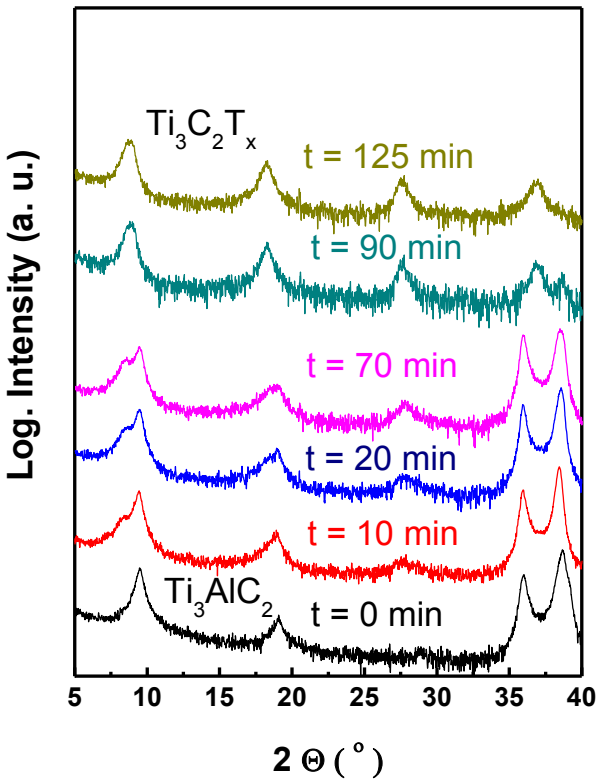


**Figure S6**. X-Ray diffraction patterns of 43-nm thick $Ti_3AlC_2$ films as a function of etching time in 50 % HF at room temperature.

## VI. EDX mapping of $Ti_3C_2T_x$

Figure S7 presents an EDX map showing the distribution of C, Ti, F, and O atoms over the corresponding high-resolution STEM image of $Ti_3C_2T_x$ produced by HF etching. The fluorine signal is concentrated primarily in the spaces between the Ti-C layers, which suggests that F atoms are attached to the surfaces of the Ti-C layers.

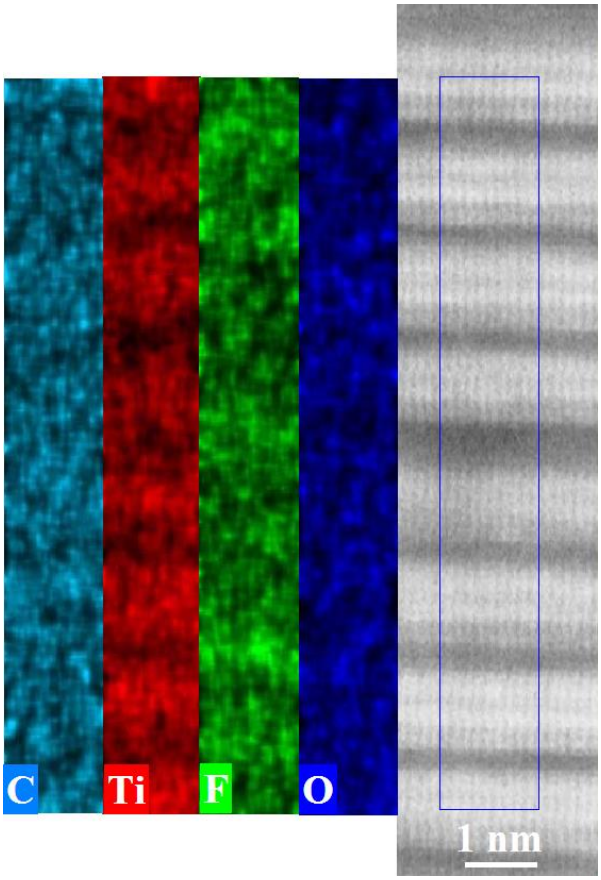


**Figure S7.** STEM image and EDX maps for $Ti_3C_2T_x$ of 60 nm nominal thickness.

## VII. Morphologies of $Ti_3AlC_2$ and $Ti_3C_2T_x$ films

Figure S8a shows the morphology of a typical $Ti_3AlC_2$ surface, where the hexagonal striations reflect to the symmetry of the basal planes together with some three-sided grains that are protruding out of plane due to their tilted orientations. Such nonbasal grains are preferentially etched, leading to premature over-etching and thus higher resistivities. Figure S8b shows the surface of $Ti_3AlC_2$ film after etching ($Ti_3C_2T_x$). Pinholes have appeared near the tilted grains in the $Ti_3C_2T_x$, presumably a result of the preferential etching of the tilted grains with respect to the grains parallel to the substrate surface.

Figures S9a,b show TEM images of the tilted grains of $Ti_3AlC_2$ and $Ti_3C_2T_x$, respectively. In Figure S9a, $Ti_3AlC_2$ grain has grown over $Ti_2AlC$. The nonbasal grain nucleated on the substrate and overgrew the basal grains, since growth along basal planes is faster than normal to it. For the $Ti_3C_2T_x$ grain (Figure S9b), defects appear in the interface between both the tilted and horizontal grains.

Low magnification cross-sectional TEM images of two $Ti_3C_2T_x$ films are shown in Figure S9c. The two samples are facing each other so that the surface of $Ti_3C_2T_x$ is

inwards. The globules appearing between the two films are carbon particles coming from the glue being used to hold the samples together on the TEM grid. The $Ti_3C_2T_x$ films

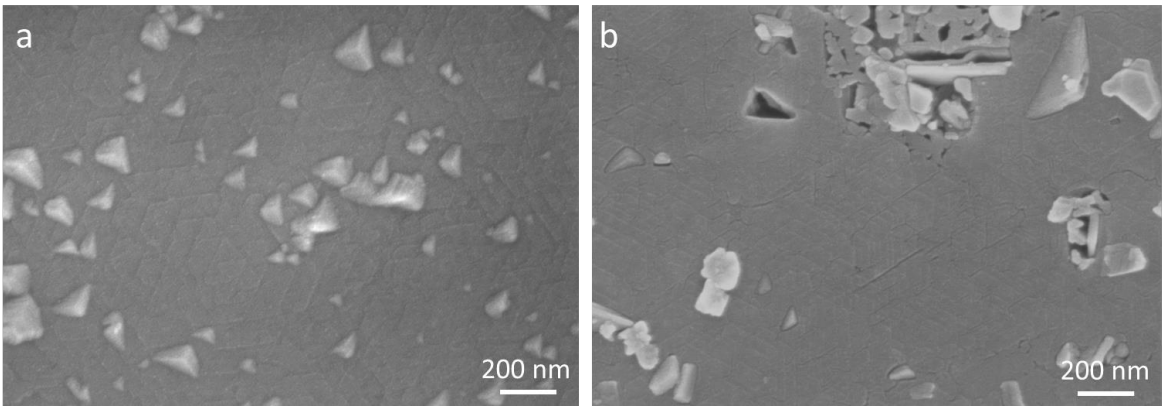


shown are uniform with some tilted grains (Figure S9a).

**Figure S8.** SEM image of $Ti_3AlC_2$ and $Ti_3C_2T_x$ of 60 nm nominal thickness.

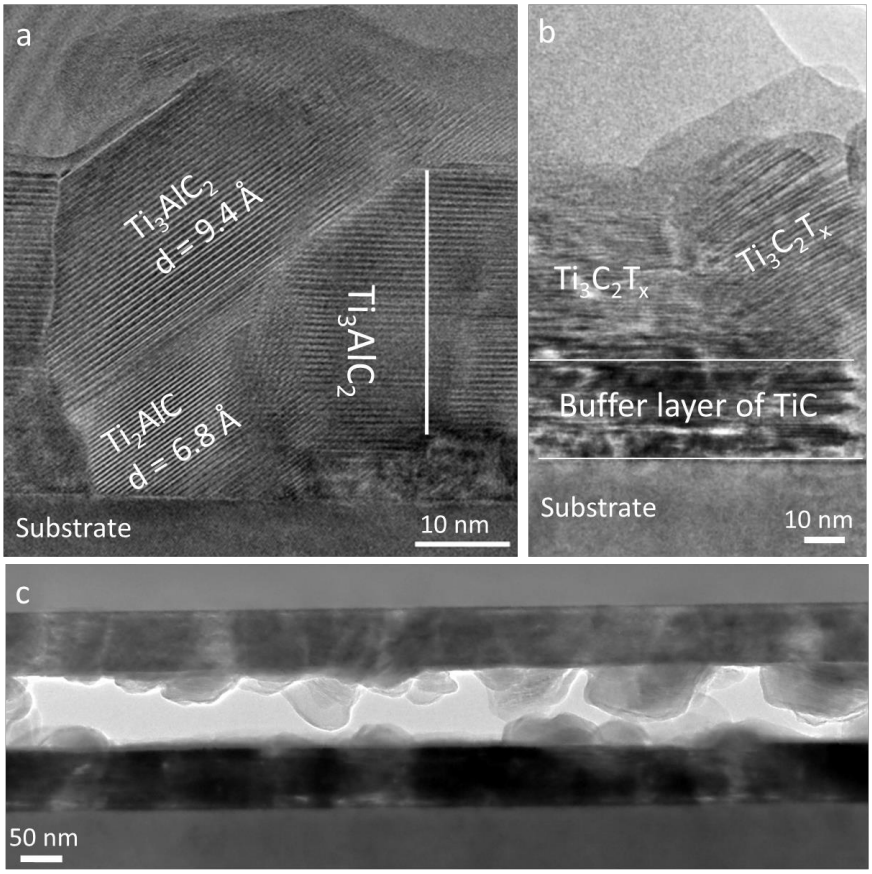


**Figure S9.** Cross-sectional TEM images of defective regions in $Ti_3AlC_2$ and $Ti_3C_2T_x$: (a) TEM image of two cross-sections of $Ti_3C_2T_x$ of 60 nm nominal thickness placed face to face. Lighter regions in the center of micrograph is the glue used during sample mounting. (b) TEM image of 60 nm thick $Ti_3AlC_2$ film grown on a sapphire substrate with TiC incubation layer showing a region not covered with TiC that ultimately resulted in a tilted grain of $Ti_3AlC_2$. (c) TEM image for $Ti_3C_2T_x$ of 60 nm nominal thickness.

## VIII. Comparison of different transparent conductive materials

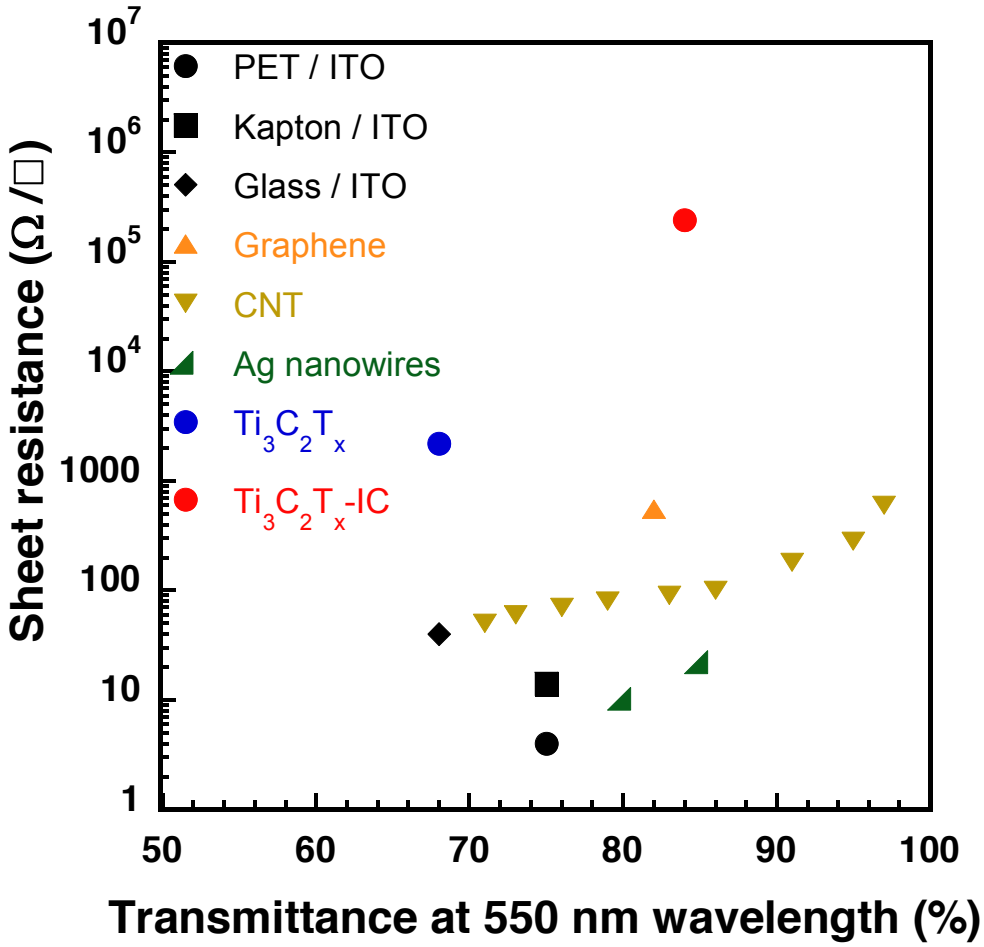


**Figure S10.** Transmittance *vs.* sheet resistance for different transparent conductors: ITO on polyethylene terephthalate (PET), Kapton® and glass;[14] black dot, square, and rhombus respectively, graphene;[15] orange triangle, carbon nanotube (CNT);[16] gold triangles, Ag nanowires;[17] green triangles, $Ti_3C_2T_x$ of 15 nm nominal thickness; blue dot and $Ti_3C_2T_x$ of 15 nm nominal thickness; red dot.

## IX. Electrical transport measurements and analysis

To understand what causes the low-temperature insulating behavior, there are numerous possible models to consider. We consider the following four models: i) thermally activated, in which case $\rho \sim \exp(E_A/kT)$; ii) 3D variable range hopping for which $\rho \sim \exp(T_0/T)^{1/4}$, iii) 2D variable range hopping for which $\rho \sim \exp(T_0/T)^{1/3}$, and, iv) a weak localization model for which $\rho \sim \ln(T)$. [18-21]

The low-temperature (< 75 K) resistivity data for $Ti_3C_2T_x$ films of 28 nm nominal thickness were fitted to all of the aforementioned models. Results of these fits are shown in Figures S10 and S11. The poor fit for the first three models to the experimental obtained (Figure S11) suggest that they can be discarded. In contradistinction, the fit for the weak-localization model is nearly perfect for all samples (insets in Figure S10). The low-temperature behavior of the resistivity is thus consistent with the weak localization model, a phenomenon typically observed in 2D metallic films.[19-21]

The negative magnetoresistance observed in the same temperature range is also consistent with the weak localization model[22]. This evidences a truly 2D behavior of the electronic transport properties of $Ti_3C_2T_x$, in that the charge carriers are confined and weakly localized within individual $Ti_3C_2T_x$ layers.

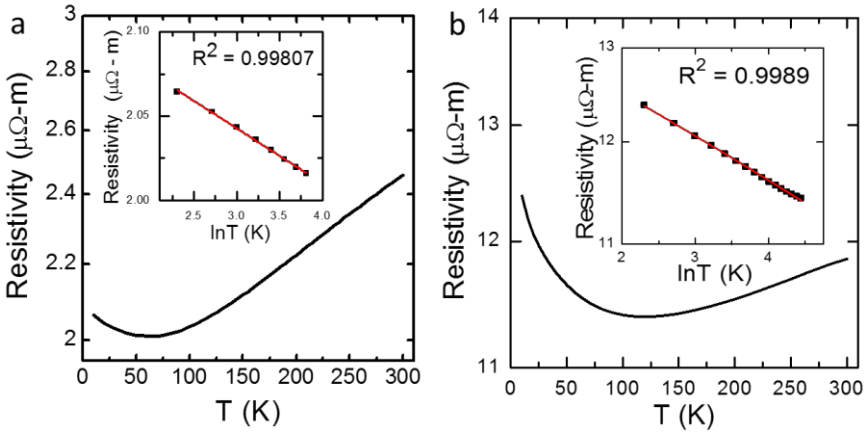


**Figure S11.** Temperature dependencies of electrical resistivities of a: (a) 60 nm thick $Ti_3C_2T_x$ film, (b) 28 nm thick $Ti_3C_2T_x$-IC film. Insets in both figures show the fits of resistivities, in the 2 to 74 K temperature range, to the weak localization model, viz. $\rho \sim \ln(T)$.

**Figure S12.** Fitting of resistivity of 28 nm nominal thickness $Ti_3C_2T_x$ films on temperature in the 2 to 74 K

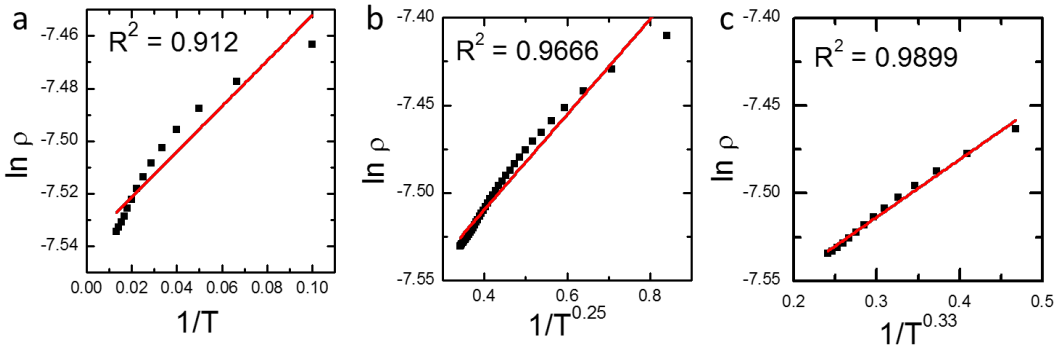


temperature range assuming: (a) a thermally activated process; (b) a 3D variable range hopping model;[18] (c) 2D variable range hopping model.[18]

REFERENCES


(1) Wilhelmsson, O.; Palmquist, J.-P.; Lewin, E.; Emmerlich, J.; Eklund, P.; Persson, P.; Högberg, H.; Li, S.; Ahuja, R.; Eriksson, O. *J. Cryst. Growth* **2006**, *291*, 290-300.
(2) Myhra, S.; Crossley, J. A. A.; Barsoum, M. W., *J. Phys. Chem. Solids* **2001**, *62*, 811-817.
(3) Mencer, D. E.; Hess, T. R.; Mebrahtu, T.; Cocke, D. L.; Naugle, D. G., *J. Vac. Sci. Technol., A* **1991**, *9*, 1610-1615.
(4) Biesinger, M. C.; Lau, L. W. M.; Gerson, A. R.; Smart, R. S. C., *Appl. Surf. Sci.* **2010**, *257*, 887-898.
(5) Jayaweera, P. M.; Quah, E. L.; Idriss, H., *J. Phys. Chem. C* 2**007**, *111*, 1764-1769.
(6) Cousens, D. R.; Wood, B. J.; Wang, J. Q.; Atrens, A., *Surf. Interface Anal.* **2000**, *29*, 23-32.
(7) Mashtalir, O.; Naguib, M.; Mochalin, V. N.; Dall'Agnese, Y.; Heon, M.; Barsoum, M. W.; Gogotsi, Y., *Nat. Commun.* **2013**, *4*, 1716.
(8) Sultana, T.; Georgiev, G. L.; Auner, G.; Newaz, G.; Herfurth, H. J.; Patwa, R., *Appl. Surf. Sci.* **2008**, *255*, 2569-2573.
(9) Yamamoto, S.; Bluhm, H.; Andersson, K.; Ketteler, G.; Ogasawara, H.; Salmeron, M.; Nilsson, A., *J. Phys.: Condens. Matter* **2008**, *20*, 184025.
(10) Ernst, K. H.; Grman, D.; Hauert, R.; Hollander, E., *Surf. Interface Anal.* **1994**, *21*, 691-696.
(11) Bourbigot, S.; Le Bras, M.; Gengembre, L.; Delobel, R. *Appl. Surf. Sci.* **1994**, *81*, 299-307.
(12) Egawa, C.; Naito, S.; Tamaru, K., *Surf. Sci.* **1983**, *131*, 49-60.
(13) Naguib, M.; Kurtoglu, M.; Presser, V.; Lu, J.; Niu, J.; Heon, M.; Hultman, L.; Gogotsi, Y.; Barsoum, M. W., *Adv. Mater.* **2011**, *23*, 4248-4253.
(14) Herrero, J.; Guillén, C., *Vacuum* **2002**, *67*, 611-616.
(15) Bae, S.; Kim, H.; Lee, Y.; Xu, X.; Park, J.-S.; Zheng, Y.; Balakrishnan, J.; Lei, T.; Kim, H. R.; Song, Y. I., *Nat. Nanotechnol.* **2010**, *5*, 574-578.
(16) Geng, H.-Z.; Kim, K. K.; So, K. P.; Lee, Y. S.; Chang, Y.; Lee, Y. H., *J. Am. Chem. Soc.* **2007**, *129*, 7758-7759.
(17) Lee, J.-Y.; Connor, S. T.; Cui, Y.; Peumans, P., *Nano Lett.* **2008**, *8*, 689-692.
(18) Yu, D.; Wang, C.; Wehrenberg, B. L.; Guyot-Sionnest, P., *Phys. Rev. Lett.* **2004**, *92*, 216802.
(19) Bergmann, G., *Phys Rev B* **1982**, *25*, 2937-2939.
(20) Bergmann, G., *Phys. Rep.* **1984**, *107*, 1-58.
(21) Shih, C.-J.; Vijayaraghavan, A.; Krishnan, R.; Sharma, R.; Han, J.-H.; Ham, M.-H.; Jin, Z.; Lin, S.; Paulus, G. L.; Reuel, N. F., *Nat. Nanotechnol.* **2011**, *6*, 439-445.
(22) Henzler, M.; Lüer, T.; Heitmann, J., *Phys Rev B* **1999**, *59*, 2383-2387.